

Effects of baryon removal on the structure of dwarf spheroidal galaxies

Kenza S. Arraki¹ * †, Anatoly Klypin¹, Surhud More^{2,3} and Sebastian Trujillo-Gomez¹

¹ *Astronomy Department, New Mexico State University, MSC 4500, P.O. Box 30001, Las Cruces, NM 88003-8001, USA*

² *Kavli Institute for Cosmological Physics, University of Chicago, 5640 S Ellis Ave, Chicago, IL 60637, USA*

³ *Kavli Institute for the Physics and Mathematics of the Universe, University of Tokyo, 5-1-5 Kashiwanoha, Kashiwa, Chiba 277 8583, Japan*

1 January 2013

ABSTRACT

Dwarf spheroidal galaxies (dSphs) are extremely gas poor, dark matter-dominated galaxies, which make them ideal laboratories to test the predictions of the Cold Dark Matter (CDM) model. We argue that the removal of a small baryonic component from the central regions of forming dSphs may substantially reduce their central dark matter density. Thus it may play an important role in alleviating one of the problems of the CDM model related with the structure of relatively massive satellite galaxies of the Milky Way. Traditionally, collisionless cosmological N -body simulations are used when confronting theoretical predictions with observations. However, these simulations assume that the baryon fraction everywhere in the Universe is equal to the cosmic mean, an assumption which can be incorrect for dSphs. We point out that the combination of (i) the lower baryon fraction in dSphs compared to the cosmic mean and (ii) the concentration of baryons in the inner part of the Milky Way halo can go a long way towards explaining the observed structure (circular velocity profiles) of dSphs. We perform controlled numerical simulations that mimic the effects of baryons. From these we find that the blowing away of baryons by ram pressure, when the dwarfs fall into larger galaxies, lowers the circular velocity profile of the satellite. In the likely scenario that baryons are blown away after the central ~ 200 – 500 pc region of the galaxies was formed, we show that the dark matter density in the central regions of dSphs declines by a factor of $(1 - f_b)^4 \approx 0.5$, where f_b is the cosmological fraction of baryons. In addition, the enhanced baryonic mass in the central regions of the parent galaxy generates tidal forces, which are larger than those experienced by subhaloes in traditional N -body simulations. Increased tidal forces substantially alter circular velocity profiles for satellites that come as close as 50 kpc. We show that these two effects are strong enough to bring the observed structure of dSphs of the Milky Way into agreement with the predictions of the subhaloes in CDM simulations, regardless of the details of the baryonic processes.

Key words: cosmology: theory – dark matter – galaxies: haloes – galaxies: dwarfs – methods: N -body simulations.

1 INTRODUCTION

According to the concordance cosmological model, a large fraction of the matter in the Universe ought to be collisionless and dark. This Cold Dark Matter (CDM) model is supported by the observed large-scale structure in the Universe, as traced by galaxies, and the emergence of this structure from the level of initial density fluctuations observed in the cosmic microwave background (e.g., Komatsu et al. 2011). However, some inconsistencies between a number of observations and the predictions of the CDM model on

small (galactic) scales have understandably produced concern and attracted a great deal of attention from both observers and theorists.

The first of the small-scale problems for the CDM model is the so-called “missing satellites problem” (Klypin et al. 1999b; Moore et al. 1999). Numerical simulations of the CDM theory predict a large number of low mass substructures to be present in a dark matter halo comparable in size to that of the Milky Way (MW). However, the number of subhaloes is much larger than the number of satellite galaxies found around MW and in the Local Group, even after accounting for the extreme low surface brightness dwarf galaxies that have been recently found using the Sloan Digital Sky Survey (Tollerud et al. 2008; Koposov et al. 2008, 2009; Bullock et al. 2010).

* NSF Graduate Research Fellow.

† E-mail: karraki@nmsu.edu

These observations of the abundance of satellite galaxies can be reconciled within the context of CDM by invoking galaxy formation physics. Star formation in low mass subhaloes can be suppressed by the heating of cold gas due to photoionization (Quinn, Katz, & Efstathiou 1996; Navarro & Steinmetz 1997; Bullock, Kravtsov, & Weinberg 2001; Somerville 2002; Benson et al. 2002; Okamoto, Gao, & Theuns 2008; Okamoto & Frenk 2009) and in larger subhaloes through energetic feedback from supernovae (e.g., Dekel & Silk 1986; Navarro, Eke, & Frenk 1996a; Kravtsov 2010; Peñarrubia et al. 2012). Thus the solution to the missing satellites problem may be in the complex physics of galaxy formation. However, it is worth noting that models with realistic and physically-motivated prescriptions remain challenging to accurately simulate due to the high numerical resolution required to capture the relevant physical processes.

A related issue is the abundance of relatively massive satellites, the so-called “too big to fail” problem – does the CDM theory predict too many satellites with large circular velocities (v_{circ})? It has been argued that the theory predicts the correct abundance of very large satellites, such as the Magellanic Clouds (Busha et al. 2011a,b), and dwarf field galaxies with $v_{\text{circ}} > 50 \text{ km s}^{-1}$ (Tikhonov & Klypin 2009; Trujillo-Gomez et al. 2011). However, the situation is different for satellites with $30 \text{ km s}^{-1} < v_{\text{circ}} < 50 \text{ km s}^{-1}$. Comparing the circular velocity profiles of subhaloes in the Aquarius N -body simulations with the circular velocities measured at the half-light radii of the bright Local Group dwarf spheroidal galaxies (dSphs), Boylan-Kolchin, Bullock, & Kaplinghat (2011, 2012) find that there are too many subhaloes. For example, haloes with $M_{\text{vir}} \sim 1.4 \times 10^{12} M_{\odot}$ have ~ 25 satellites with infall circular velocities $v_{\text{circ}} > 30 \text{ km s}^{-1}$ within 300 kpc of the halo’s centre (Boylan-Kolchin et al. 2012). In a given halo, at least seven of these satellites do not have observed MW counterparts, so the simulations contain too many very compact, large subhaloes.

There are a couple of solutions, within the context of the CDM model, that can explain some of these inconsistencies. First and foremost, the CDM cosmology adopted for the Aquarius haloes uses $\sigma_8 = 0.9$ instead of the lower concordance value of $\sigma_8 = 0.8$. Subhaloes in lower σ_8 models have lower abundances and their density profiles are less concentrated, such that they are more susceptible to tidal effects (Di Cintio et al. 2011). Secondly, the abundance of substructures above a certain circular velocity scales linearly with the host halo mass. Lowering the mass of the MW by ~ 20 per cent (i.e., from $M_{\text{vir}} \sim 10^{12} M_{\odot}$ to $M_{\text{vir}} \leq 8 \times 10^{11} M_{\odot}$) can reduce the abundance of the massive, dense subhaloes to a number low enough so that the absence of such satellites around the MW can simply be attributed to a statistical fluke (Wang et al. 2012).

The other possibility is that baryonic processes, such as stellar feedback and photoionization, in combination with the subsequent tidal stripping of their outer regions, impacts the inner structure of massive subhaloes. This could result in the generation of cores in their central density profiles and simultaneously solve the massive failures problem (Mashchenko, Couchman, & Wadsley 2006; Mashchenko, Wadsley, & Couchman 2008; Governato et al. 2010; Peñarrubia et al. 2010; Di Cintio et al. 2011; Pontzen & Governato 2012; Governato et al. 2012; Parry et al. 2012; Zolotov et al. 2012; Brooks & Zolotov 2012; Brooks et al. 2012; Peñarrubia et al. 2012). However, capturing the baryonic processes accurately requires numerical simulations with hydrodynamics to be run at resolutions of tens of parsecs, which are difficult to achieve. Ques-

tions also remain about the sub-grid models implemented to mimic baryonic processes and the magnitude of the resulting feedback (Ceverino & Klypin 2009; Colín et al. 2010).

If the discrepancies between predictions of the CDM model and observations listed above are not resolved with realistic baryonic effects, then these observations will provide a unique opportunity to probe the nature of dark matter. Alternative scenarios, such as warm dark matter or self-interacting dark matter, have been proposed to explain the differences between the CDM model predictions and observations (Lovell et al. 2012; Vogelsberger, Zavala, & Loeb 2012).

In this paper, we investigate modifications to the CDM expectations induced by the presence of baryons. We focus on well-established and undisputed facts about the behaviour of baryons in the MW, namely (i) that the fraction of mass in baryons within subhaloes that host dSphs is substantially below the cosmic mean and (ii) that there is a baryonic concentration within the central parts of the MW halo.

Cosmological N -body simulations of large-scale structure are initialised taking into account the effect of baryons on matter fluctuations. However, while evolving this simulation forward in time, the simplifying assumption that all matter, including baryonic matter, is collisionless, is commonly used. This implies that the baryonic distribution follows the matter distribution in an unbiased manner. Although this assumption works well if one wants to calculate large-scale properties of the mass distribution (scales larger than typical haloes), the predictions of such simulations on smaller scales must be interpreted with caution. Gas poor objects, like dSphs, should have larger dark matter masses than baryonic masses, while the central parts of the MW should have more baryonic mass than it is assigned in simulations.

This simplifying assumption leads to a twofold effect, causing the dSphs to be more resistant to tidal stripping in conventional N -body simulations than in reality. The density of dSphs in the inner regions is larger in traditional N -body simulations than what it should be, given the loss of baryonic material. At the same time, the density in the central regions of the parent halo is underestimated. In reality, baryons lose energy through radiation and fall to the centre of the parent halo which makes their interiors more massive. In N -body simulations, this is neglected because the baryons are assumed to be collisionless, similar to dark matter. This implies that the tidal forces that act on the subhaloes that host the dSphs are weaker in these simulations than in reality. This causes massive subhaloes to preserve their structure and high circular velocities, allowing them to survive in simulations down to redshift zero.

The paper is organized as follows. We discuss different aspects of dSph galaxies and possible scenarios for their formation in Section 2. In Section 3, we present the details of our simulations and analytical methods. The effects of baryon removal for isolated galaxies are studied in Section 4. In Section 5, we present results of tidal stripping models, and conclusions are given in Section 6.

2 FORMATION AND EVOLUTION OF DWARF SPHEROIDALS

The origin of dSphs is, as yet, unknown with current formation scenarios constrained by simulations and by observations of dwarfs in the Local Group. In order to address why dSphs have a lower baryonic fraction than the cosmic mean, we must examine their formation and evolution. This information will guide us when we set the parameters of dwarf galaxies in our simulations.

The radial distribution of satellites may provide valuable information on the evolutionary history of dSphs. It is known that 95 per cent of dSphs are located within distances of 250 kpc from the centres of known groups (e.g., Karachentsev 2005; Karachentsev, Karachentseva, & Sharina 2005). In other words, there are hardly any isolated dSphs. Even inside the Local Group the dSphs are preferentially found in the inner regions around the MW and M31. These results imply that there are unique environmental forces altering the majority of dSph morphologies.

A possible mechanism for forming dwarf galaxies is through the smallest “baryonic building blocks,” which are 3σ fluctuations at $z \sim 10$, on the order of $10^8 M_\odot$. Haloes with $M \lesssim 2 \times 10^7 M_\odot$ are unable to retain their gas when SNe feedback and reionization are introduced, but the remaining structures with $M \gtrsim 2 \times 10^7 M_\odot$ do retain their gas (see Peebles 1984; Ricotti & Gnedin 2005; Gnedin & Kravtsov 2006; Moore et al. 2006; Read, Pontzen, & Viel 2006a; Peñarrubia et al. 2010, for a discussion of the critical mass scale and star formation thresholds). When these smallest luminous structures remain far from potential perturbers, they retain their gas and form stars, matching the field dwarf irregular (dIrr) population. The satellites with pericentric passages close to their host are subject to ram pressure stripping, which removes the gas and inhibits star formation.

A formation scenario that naturally recovers the radial distribution of dSphs is termed “tidal stirring” (Mayer et al. 2001). The tidal stirring mechanism relies on the existence of field dIrr galaxies that begin discy and gas rich and enter the gravitational potential of a massive host before $z \sim 1$. Most of the dwarf’s gas content is lost via ram pressure stripping, hindering future star formation (e.g., Eskridge 1988; Grebel, Gallagher, & Harbeck 2003). The morphology of the dwarf is changed by tidal forces; the disc transforms into a spheroidal component due to bar instabilities created by tidal shocks (see Mayer et al. 2001; Mayer 2005; Mayer et al. 2007; Klimentowski et al. 2007, 2009, 2010; Lokas et al. 2010; Kazantzidis et al. 2011, and references therein for details). More recently accreted dwarfs ($z < 1$) may have a portion of their gas removed, with the remainder used in bursty star formation events as they pass close to the host throughout their orbit. Baryonic mass loss may be completed within a few million years, if the feedback is quite strong, or over hundreds of millions of years, as each feedback episode removes more mass and decreases the depth of the galaxy’s potential well.

If some dwarfs existed within groups before they were accreted by a primary halo, they could have undergone significant additional mass loss. The existence of such a grouping before infall is under discussion for the Local Group dwarfs (see D’Onghia & Lake 2008; Li & Helmi 2008; Metz et al. 2009; Klimentowski et al. 2010). This means that the gas poor dSphs we currently observe may have undergone disruption for an even longer time period than expected. These interactions between dwarfs can lead to a factor of two decrease in v_{\max} and significant mass loss (Kravtsov, Gnedin, & Klypin 2004; Diemand, Kuhlen, & Madau 2007; Madau, Diemand, & Kuhlen 2008; Klimentowski et al. 2009).

The inner density profile of the dwarf, the orbital parameters, the inclusion of a baryonic disc in the host, and the mass ratio of dwarf to host galaxy all impact the severity of stripping that a satellite undergoes. Stronger inner density cusps result in dwarfs that persist even after undergoing the most extreme tidal stripping (Colpi, Mayer, & Governato 1999; Peñarrubia, McConnachie, & Navarro 2008a; Peñarrubia, Navarro, & McConnachie 2008b; Peñarrubia et al.

2010). The inclusion of a disc component in the host can decrease the masses of satellites by an order of magnitude as well as the total number of subhaloes at redshift zero by a factor of two or three, depending on the ratio of host virial mass to disc mass (Peñarrubia et al. 2010; D’Onghia et al. 2010).

Much work has been done quantifying the effects of tidal stripping and heating (e.g. Gnedin, Hernquist, & Ostriker 1999; Taylor & Babul 2001; Taffoni et al. 2003; Read et al. 2006b,c; Peñarrubia et al. 2009; D’Onghia et al. 2010). Tidal heating is important for orbits with pericentres within 20 kpc, while disc shocking dominates for pericentres within 12 kpc. However, when a disc is present, orbits with pericentres within 20 kpc are completely destroyed, except those with the largest inner density profiles. The most massive satellites ($M_{\text{sat}}/M_{\text{host}} \gtrsim 0.1$) sink quickly due to dynamical friction and merge with the host, whereas the least massive satellites ($M_{\text{sat}}/M_{\text{host}} \lesssim 0.02$) have no change in their orbital parameters but undergo significant mass loss.

Both internal and environmental effects strongly influence the mass assembly history of a dwarf galaxy. This can result in dramatically different density profiles for galaxies of the same total mass. Due to the lack of certainty in how these haloes assembled, we test a variety of methods to remove the baryonic component of dSphs.

3 METHODOLOGY

3.1 Cosmological hydrodynamical simulation

Realistic estimates of how a satellite’s mass distribution changes due to the removal of baryons can be obtained by running cosmological hydrodynamical simulations. To this extent, we ran cosmological simulations of a dwarf galaxy with $M_{\text{vir}} = 3 \times 10^{10} M_\odot$ with the same initial conditions twice, once without gas removal and the other time with the gas blown away just before $z = 1$.

To perform the simulations, we used the adaptive mesh refinement N -body+hydrodynamics code *hydroART* (Kravtsov, Klypin, & Khokhlov 1997; Kravtsov 1999). The code is adaptive in both space and time, achieving higher resolution in regions of higher mass density. We used the following cosmological parameters: $\Omega_M = 1 - \Omega_\Lambda = 0.27$, $\Omega_b = 0.04$, and $\sigma_8 = 0.8$. The simulation zoomed in on a single halo inside a $10 h^{-1} \text{Mpc}$ comoving box and achieved a maximum resolution of 60 pc and a DM particle mass $m_p \sim 10^5 M_\odot$ at redshift zero.

The physical model used by the code includes many relevant processes, such as cooling down to 300 K from metals and molecules, a homogeneous UV background, metal advection, and stellar mass loss. Star formation occurred stochastically in regions where the gas density reached a critical threshold, $n_{\text{SF}} > 1 \text{ cm}^{-3}$, with a constant efficiency, $\epsilon_{\text{SF}} = 2.5$ per cent. Each “star” particle represented a simple stellar population with a Chabrier IMF and deposited thermal energy via SNe and stellar winds as well as radiation pressure from O and B stars into the surrounding ISM.

This model is based on observations of star forming regions. More details on the implementation of the star formation and feedback model can be found in Trujillo-Gomez, S. et al. (in prep). The isolated dwarf galaxies simulated using this new model are in very good agreement with observations. In particular, they have no bulges, slowly rising rotation curves, and constant or slowing increasing star formation histories.

We created two isolated dwarf galaxies. The first run, the fiducial run, was performed as described above with no alterations. We also ran a second simulation, which we call the “no gas” run. It is

Table 1. Mass values for the *hydroART* simulated galaxies. Two isolated dwarfs were run, one fiducial model (left) and one where all gas within the galaxy was removed 200,000 years before $z = 1$ (right). The fiducial model increases its stellar mass and accretes more gas; however, the no gas dwarf retains only a hot diffuse gas component. The stellar mass in the no gas model is reduced from $z = 1$ to $z = 0$ due to stellar mass loss, while the virial masses do not increase substantially from $z = 1$ to $z = 0$ for either model.

| Model | fiducial | | | no gas | | |
|---------|-------------------------------------|---|--|-------------------------------------|---|--|
| | M_{vir} (M_{\odot}) | $M_{\text{gas}}(r < 10 \text{ kpc})$ (M_{\odot}) | $M_{*}(r < 10 \text{ kpc})$ (M_{\odot}) | M_{vir} (M_{\odot}) | $M_{\text{gas}}(r < 10 \text{ kpc})$ (M_{\odot}) | $M_{*}(r < 10 \text{ kpc})$ (M_{\odot}) |
| $z = 1$ | 2.3×10^{10} | 6.7×10^8 | 5.4×10^7 | 2.2×10^{10} | 6.2×10^3 | 5.4×10^7 |
| $z = 0$ | 3.0×10^{10} | 6.4×10^8 | 3.0×10^8 | 2.5×10^{10} | 6.2×10^3 | 4.9×10^7 |

the same as the fiducial run until just before $z = 1$, when we removed the gas in the model to emulate the gas stripping that occurs as a satellite falls into its host halo. To achieve this, we artificially increased the temperature of all the gas in the high-resolution region to 10^6 K and halted cooling in those cells from $z = 1$ until $z = 0$. This removed the majority of the gas mass, with all bound gas existing as a hot diffuse medium. Only $\sim 6000 M_{\odot}$ of gas remained in the galaxy with a total of $\sim 10^6 M_{\odot}$ of gas within the virial radius of the halo. Since this gas could not cool, the galaxy was unable to form any more stars.

These simulations do not include the effects of tidal stripping of DM and stars by the host potential, and as such, they provide an estimate of the minimum effect of baryonic physics on the DM density profiles. Table 1 summarises the properties of the two models. In Section 4, we will use the results of these simulations to test our model for adiabatic expansion of the halo due to the baryonic loss.

3.2 *N*-body simulations

We performed controlled collisionless *N*-body simulations to quantify the gravitational effect of the removal of baryons from subhaloes and the enhanced tidal effects on subhaloes from the Milky way disc. In what follows, we describe the code and the initial conditions we used. These simulations incorporated the undisputed net results of baryonic processes.

3.2.1 Code and initial conditions

We used a direct summation *N*-body code with the leapfrog time-stepping integration scheme, a constant time step $\Delta t = 6.4 \times 10^5$ yrs, and a Plummer softening of $\epsilon = 20$ pc. All resultant simulations retained an energy conservation of $\Delta E/E < 10^{-5}$. The code was run in parallel by using both OMP (Open Multi-Processing) and MPI (Message Passing Interface) libraries.

Initial conditions were set up by solving the equilibrium Jean's equation to obtain the rms velocity dispersion $v_{\text{rms}}(r)$ as a function of radius for a dwarf with a spherical Navarro, Frenk, & White (1996b, 1997, NFW profile hereafter) density distribution given by

$$\rho_{\text{sat}}(r) = \frac{v_{\text{max}}^2}{4\pi G r_s^2} \frac{x_{\text{max}}}{\mu(x_{\text{max}})} \frac{1}{x(1+x)^2}, \quad x \equiv r/r_s, \quad (1)$$

$$\mu(x) = \ln(1+x) - \frac{x}{(1+x)}. \quad (2)$$

Here v_{max} is the maximum circular velocity of the dwarf and x_{max} is the distance at which the velocity peaks, where $x_{\text{max}} = 2.163$.

The distribution was truncated at the outer radius $r_{\text{out}} = 16r_s$. This truncation radius is close to the expected virial radius for haloes with masses typical for large satellites of the Milky Way.

The exact value of r_{out} is unimportant because the satellite will be severely tidally stripped when it falls into the potential well of the MW.

When setting initial conditions, we used multiple masses for particles. In the inner regions, the particle mass, m_1 , was small and nearly constant. The mass increased with distance as

$$m_1(r) = m_1(0) \left[1 + \left(\frac{r}{r_s} \right)^2 \right], \quad (3)$$

where $m_1(0)$ is a normalisation constant. This prescription allowed us to resolve the central region of the dwarf with small particles and at the same time have an extended halo. Throughout the dwarf's evolution, particles of different mass moved in radius so that massive particles occasionally came to the centre. We monitored the situation and found that the central ~ 1 kpc region was always dominated by very small particles with a very low contribution of more massive particles. As an example we quote results from a 200,000 particle simulation after 10 dynamical times. Within the central 100 particles, the average particle mass increased by just 2 per cent. Inside the radius of the first 1000 particles, the mass per particle increased by 6 per cent.

We assumed an isotropic Gaussian distribution of velocities. Gaussian velocities produce small non-equilibrium effects for the NFW distribution. We allowed the system to evolve in isolation for 10 dynamical times to settle and come into equilibrium. Non-equilibrium effects were small at any moment. For example, after 10 dynamical times, the maximum circular velocity was within 2 per cent of initial value. The largest effect was a decline in the density, which occurred at the very centre. The density in the central ~ 100 pc declined by about 30 per cent. We used the evolved configuration as the reference when we examined the results of other simulations. Overall, these changes were at a low enough level for the density and circular velocities to retain their basic NFW shape and cusp.

Our simulations consisted of 200,000 particles of various mass. If we had used a constant mass per particle, we would have needed $N_{\text{eff}} = 1.3 \times 10^6$ particles to resolve the central region with the same small particles.

The gravitational force of the MW acting on satellites was modelled using frozen external potentials, which roughly approximated the mass distribution in our MW galaxy.

3.2.2 Scaling models

When scaling *N*-body simulations to physical units, we chose the radius (r_0) and velocity (v_0) to be our free parameters, which left all other quantities, such as time-scale (t_0) and mass (m_0), dependent on the choice of radius and velocity scales.

Our simulated dwarfs were created to test the effects of baryon

removal and tidal stripping for large satellites. The initial dwarf has the following properties: $r_s = 4.0$ kpc and $v_{\max} = 62 \text{ km s}^{-1}$. This maximum circular velocity is somewhat high for dSphs. However, these parameters were chosen to mimic the high end of the “massive failures” (Boylan-Kolchin et al. 2012) before infall. Similar to the results of Boylan-Kolchin et al. (2012), the entire initial profile of our dwarf is inconsistent at 2σ with all the dSphs in the Local Group. This initial setup allows us to test if an extreme case for a dwarf satellite is able to reproduce observations by including baryonic effects.

Our host galaxy was matched to the Aquarius E galaxy virial dark matter mass with an added baryonic component. The host galaxy is defined as: $r_{\text{disc}} = 3$ kpc, $M_{\text{disc}} = 6.05 \times 10^{10} M_{\odot}$, $r_s = 25.12$ kpc and $M_{\text{vir}} = 1.39 \times 10^{12} M_{\odot}$ ($v_{\text{circ}} = 179 \text{ km s}^{-1}$). These are reasonable values for the MW halo and disc mass, which are estimated to be $M_{\text{tot}} = 0.7 - 3 \times 10^{12} M_{\odot}$ (Wilkinson & Evans 1999; Sakamoto, Chiba, & Beers 2003; Smith et al. 2007; Li & White 2008; Xue et al. 2008; Kallivayalil et al. 2009; Guo et al. 2010; Watkins, Evans, & An 2010) and $M_{\text{disc}} \sim 5.5 \times 10^{10} M_{\odot}$ (Gerhard 2002; Flynn et al. 2006), respectively.

We calculated the circular velocity of the initial perturber at 8 kpc, to provide the reader with a comparison of the halo and the MW. Using the mass within a given radius equation for the exponential disc and the NFW profile, we found that the baryon values are $M_{\text{bar}}(r < 8 \text{ kpc}) = 4.5 \times 10^{10} M_{\odot}$ or a $v_{\text{circ}} = 156 \text{ km s}^{-1}$ and the DM values are $M_{\text{DM}}(r < 8 \text{ kpc}) = 4.9 \times 10^{10} M_{\odot}$ or a $v_{\text{circ}} = 162 \text{ km s}^{-1}$. After summing the circular velocities in quadrature we obtained $v_{\text{circ}} = 224 \text{ km s}^{-1}$. This is close to the circular velocity of the solar neighbourhood $v_{\text{circ}}(R_0) = 218 \pm 6 \text{ km s}^{-1}$, as found by Bovy et al. (2012).

3.2.3 Setup of tidal stripping simulations

The simulations were run in the presence of an external MW-sized perturber after running in isolation. The no mass removal case (NR) was run with a pure NFW perturber, while all other cases were run with a NFW plus spherical exponential “disc” perturber. This setup allows the NR case to remain as the pure DM example, while the mass removal cases show the effects of including baryons (by adding a disc) in the simulation (see Table 2 for naming conventions).

All satellites were run in circular orbits at $r_{\text{orbit}} = 50$ kpc, 70 kpc, 100 kpc, and 150 kpc to examine the most extreme effects of tidal stripping from different distances. Elliptical orbits were also run to give more realistic results of tidal stripping. We created orbits with varying eccentricities by changing apocentre and pericentre distances from 1:2 to 1:5 to compare the effects of different subhalo orbital evolutionary histories. These orbits are less elliptical than the typical orbital ratio of 1:6 derived by Ghigna et al. (1998); however, they are well within the 90 per cent interval found by Diemand et al. (2007), which extends from $\sim 1:28$ to $\sim 2:3$ orbits.

In the Via Lactea simulations (Diemand et al. 2007), almost all galaxies within the “earliest forming substructure” sample had orbits that fell within 30 kpc of the host. In the SPH simulations run by Zolotov et al. (2012), over half of all the subhaloes had orbits with pericentres below 30 kpc (private communication). In our truncation radius estimates (Section 5.1), we find that a satellite in the presence of a MW with a baryonic disc component should have interesting tidal evolution if it exists in an orbit with pericentre ~ 40 kpc. This occurred when the truncation radius, r_t , had values from 2 to 4 times the scale radius, r_s . We ran four elliptical orbits.

Table 2. Different dwarf galaxy cases. The initial and final maximum circular velocities during their isolated runs are listed.

| Label | Description | $v_{\max,i}$ | $v_{\max,f}$ | $\frac{v_{\max,f}}{v_{\max,i}}$ |
|-------|----------------------------|--------------|--------------|---------------------------------|
| NR | no baryonic mass removal | 62.1 | 64.2 | 1.03 |
| PR | pre-halo formation removal | 64.2 | 57.6 | 0.90 |
| ER | exponential removal | 64.2 | 51.2 | 0.80 |
| IR | instantaneous removal | 64.2 | 51.0 | 0.79 |

Table 3. Orbital parameters for each satellite galaxy. Included are their initial maximum circular velocities and final maximum circular velocities after 5 Gyrs. Labels that end in “c” denote a circular orbit and those that end in “e” denote an elliptical orbit.

| Label | Description | $v_{\max,i}$ | $v_{\max,f}$ | $\frac{v_{\max,f}}{v_{\max,i}}$ |
|--------|-------------------------|--------------|--------------|---------------------------------|
| NR150c | NR, 150 kpc orbit | 64.2 | 60.7 | 0.95 |
| NR100c | NR, 100 kpc orbit | 64.2 | 57.2 | 0.89 |
| NR70c | NR, 70 kpc orbit | 64.2 | 51.6 | 0.80 |
| NR50c | NR, 50 kpc orbit | 64.2 | 43.0 | 0.67 |
| NR1:2e | NR, 150 to 70 kpc orbit | 64.2 | 56.5 | 0.88 |
| NR1:3e | NR, 150 to 50 kpc orbit | 64.2 | 53.8 | 0.84 |
| NR1:5e | NR, 150 to 30 kpc orbit | 64.2 | 51.2 | 0.80 |
| NR1:4e | NR, 120 to 30 kpc orbit | 64.2 | 46.9 | 0.73 |
| PR150c | PR, 150 kpc orbit | 57.6 | 53.6 | 0.93 |
| PR100c | PR, 100 kpc orbit | 57.6 | 49.5 | 0.86 |
| PR70c | PR, 70 kpc orbit | 57.6 | 42.1 | 0.73 |
| PR50c | PR, 50 kpc orbit | 57.6 | 28.1 | 0.49 |
| PR1:2e | PR, 150 to 70 kpc orbit | 57.6 | 48.5 | 0.84 |
| PR1:3e | PR, 150 to 50 kpc orbit | 57.6 | 44.7 | 0.78 |
| PR1:5e | PR, 150 to 30 kpc orbit | 57.6 | 40.4 | 0.70 |
| PR1:4e | PR, 120 to 30 kpc orbit | 57.6 | 34.2 | 0.59 |
| ER150c | ER, 150 kpc orbit | 51.2 | 46.0 | 0.90 |
| ER100c | ER, 100 kpc orbit | 51.2 | 40.5 | 0.79 |
| ER70c | ER, 70 kpc orbit | 51.2 | 30.0 | 0.59 |
| ER50c | ER, 50 kpc orbit | 51.2 | 10.7 | 0.21 |
| ER1:2e | ER, 150 to 70 kpc orbit | 51.2 | 39.6 | 0.77 |
| ER1:3e | ER, 150 to 50 kpc orbit | 51.2 | 34.8 | 0.68 |
| ER1:5e | ER, 150 to 30 kpc orbit | 51.2 | 29.9 | 0.58 |
| ER1:4e | ER, 120 to 30 kpc orbit | 51.2 | 22.5 | 0.44 |
| IR150c | IR, 150 kpc orbit | 51.0 | 45.8 | 0.90 |
| IR100c | IR, 100 kpc orbit | 51.0 | 39.9 | 0.78 |
| IR70c | IR, 70 kpc orbit | 51.0 | 29.0 | 0.57 |
| IR50c | IR, 50 kpc orbit | 51.0 | 10.6 | 0.21 |
| IR1:2e | IR, 150 to 70 kpc orbit | 51.0 | 39.0 | 0.76 |
| IR1:3e | IR, 150 to 50 kpc orbit | 51.0 | 34.0 | 0.67 |
| IR1:5e | IR, 150 to 30 kpc orbit | 51.0 | 29.2 | 0.57 |
| IR1:4e | IR, 120 to 30 kpc orbit | 51.0 | 21.4 | 0.42 |

Three of the four orbits had the same apocentre and are listed here: 1:2e (150–70 kpc), 1:3e (150–50 kpc), and 1:5e (150–30 kpc). The fourth orbit, 1:4e (120–30 kpc), had a different ellipticity but arrived at the same 30 kpc pericentre as the 1:5e orbit. A description of each dwarf galaxy’s orbits is provided in Table 3.

3.3 Adiabatic expansion

The removal of baryons within a galaxy results in smaller mass inside a given radius r . In turn, this reduces the force of gravity and causes the galaxy to expand. This is a known and qual-

itatively well understood physical process (Zeldovich et al. 1980; Blumenthal et al. 1986; Gnedin et al. 2004). It is also observed in many cosmological simulations that include hydrodynamics and star formation (Gustafsson, Fairbairn, & Sommer-Larsen 2006; Colín, Valenzuela, & Klypin 2006; Tissera et al. 2010; Gnedin et al. 2011). Here we use the simplest prescription of Blumenthal et al. (1986) to make an analytical model for the expansion of a galaxy when it loses mass. It assumes circular orbits for dark matter particles and uses the conservation of angular momentum to derive a relation between the initial mass, $M_i(r_i)$, and radius, r_i , and the final mass, $M_f(r_f)$, and radius, r_f . Note that the prescription does not use adiabatic invariants; it uses an integral of motion – the angular momentum. Thus its limitation is not that the process must be slow (adiabatic), it is the assumption of circular motions. An extension of the prescription, provided by Gnedin et al. (2004), makes a correction due to non-circular motions. As Gnedin et al. (2004) shows, in the regime of small compression (or expansion) the difference between the two approximations is small.

It is convenient to rewrite the Blumenthal et al. (1986) prescription using the circular velocity, $V_{\text{circ}} = \sqrt{GM(r)/r}$ of a mass shell, where $M(r)$ is the mass inside radius r . If $\alpha(r_i)$ is the fraction of mass that remains inside r_i after the removal of baryons, then the final radius, r_f , and circular velocity, V_f , are given by

$$r_f = \frac{r_i}{\alpha(r_i)}, \quad (4)$$

$$V_f(r_f) = \alpha(r_i) V_i(r_i) = \alpha(\alpha r_f) V_i(\alpha r_f). \quad (5)$$

Note that the factor of α in equation (5) enters linearly in both the radius, r_i , and circular velocity, V_i . As a result, the effect of the expansion is rather large. This should be contrasted with the case that lacks expansion when mass $M(r)$ decreases by a factor of α but the radius stays the same: $r_f = r_i$. In this case, the final circular velocity, V_f , declines only by a factor of $\sqrt{\alpha}$, which is a small effect. For the baryon removal case, where $f_b \approx 0.17$ (Komatsu et al. 2011), we find a ~ 10 per cent change, where it is expected that $\alpha \approx 1 - f_b$.

3.4 A tidal stripping model

Simulations of the effects of tidal stripping can be very demanding and take substantial computing resources. It is helpful to have a simple model that can reproduce some of the simulation results. We found that the following model produces quite accurate results. The motivation is simple; after the removal of some fraction of mass due to tidal forces, the halo expands and some particles may become unbound giving rise to another round of mass loss. Note that this happens because dark matter particles move on elliptical orbits, which are typically very elongated. Thus the removal of mass from the peripheral regions, where the tidal force is strong, leads to a lack of mass in the inner regions over time. Therefore, even the central region of a halo may be affected by the tidal stripping.

A realisation of the NFW distribution was made using the prescription described in Section 3.2.1. For this model we increased the number of particles to 500,000, which provided many low mass particles in the central region of the dwarf. This allowed us to make detailed calculations of tidal stripping without numerical errors.

After the dwarf was created, we estimated the energy of each particle and removed all unbound particles. When estimating the potential energy of a particle, we included the potential associated with a spherically symmetric tidal force. Only particles inside the

tidal radius were used for calculations of the gravitational potential of the dark matter itself.

The initial tidal radius, r_t , was parametrised by its ratio to the characteristic radius, r_s . This set the normalisation for the tidal potential, which did not change when we proceeded with iterations of tidal stripping.

Once the unbound particles were removed, the halo was adiabatically expanded following equations (4) and (5). Following this method, we found the mass of bound particles within each radius and compared it with the mass at the previous iteration. The ratio of these masses gave the α parameter, which was then used for the adiabatic expansion; the coordinates were increased and the velocities were decreased according to equations (4) and (5). We also found the new tidal radius and proceeded with the next round of removal of unbound particles.

Just like in our N -body simulations, we found that tidal stripping continuously removed mass from the halo. In other words, there was no convergence, and some fraction of mass was removed even after many iterations. However, the rate of the mass removal dramatically depended on the initial tidal radius. We found very little effect when the initial tidal radius exceeded $r_t = 4r_s$. At smaller tidal radii, the rate of stripping increased. By comparing the simple model to the N -body simulations, we found that between 10 and 30 iterations gave results very similar to those observed in actual simulations.

4 EFFECTS OF BARYON REMOVAL

4.1 Effects of baryon removal in hydrodynamical simulations: testing the adiabatic expansion model

In this section, we examine the effects of infall and gas removal on the dark matter mass distribution of a dwarf galaxy. We modelled this process in detail by performing two high resolution cosmological simulations of the formation and evolution of a dwarf galaxy, including gas, star formation, and feedback.

The fiducial run was done with no removal of gas – the system evolved without any intervention – and mimics the evolution of a dIrr galaxy. As the left panel of Fig. 1 demonstrates, the simulation reproduces some generic properties of dIrrs: almost no bulge, gently rising rotation curve and a large mass in gas as compared with the stellar mass. The model does have an issue related with the strong stellar feedback used for the simulation; the fraction of mass in baryons is a factor of two too low. In this simulation, there are $\sim 0.5f_b$ the central region, $r < 5$ kpc, while observations point to a larger value, closer to the cosmological fraction (Oh et al. 2011). In the second run, the gas was removed from the halo just before $z = 1$ and evolved to $z = 0$, without allowing the gas component to cool.

Note that the total circular velocity profile of the fiducial run does not change appreciably from $z = 1$ to $z = 0$, without intervention. There was little evolution in total mass in the outer regions of the dwarf; in contrast, within the inner 500 pc, the mass decreased slightly. The lack of evolution in the fiducial isolated dwarf over this time period, with the exception of continued star formation, makes this particular halo a good test of the adiabatic expansion model against a simulation with gas removal.

Fig. 1 compares the fiducial and no gas removal models. Removal of gas clearly resulted in the expansion of the halo, with the circular velocity declining at every radius. The fraction of mass removed at $z = 1$ is small; within the central 5 kpc region, the

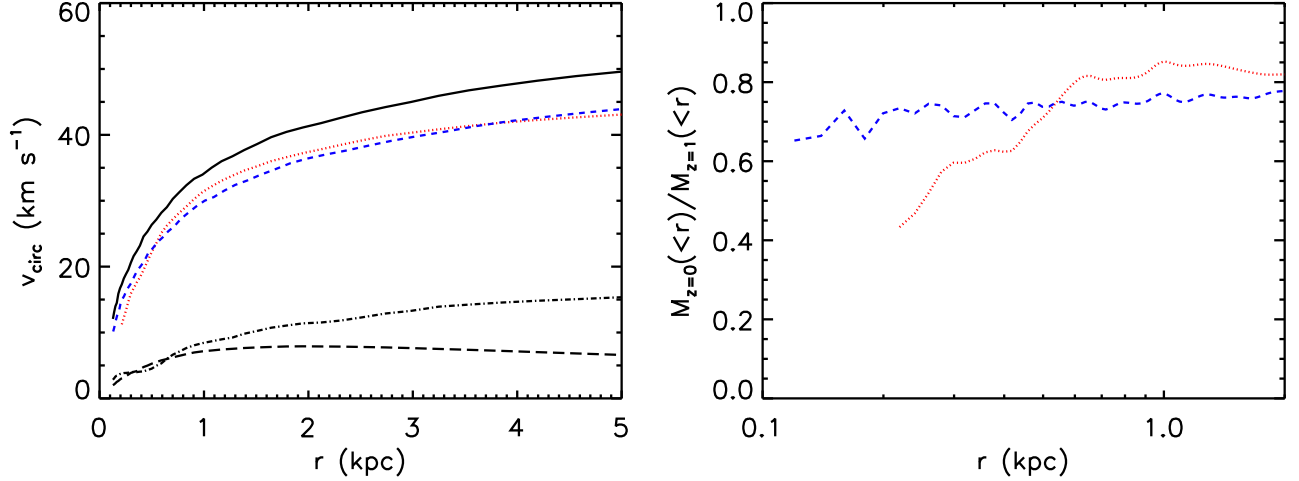


Figure 1. Results from the cosmological hydrodynamical simulations displaying the effects of gas removal from an isolated dwarf galaxy. *Left:* The circular velocity profile of the fiducial model at $z = 1$ is shown as the solid line. The dotted (red) curve shows the gas removal simulation results at $z = 0$. The short-dashed (blue) curve is for the adiabatic expansion model. The bottom curves represent the circular velocity profiles of the gas (dot-dashed curve) and stars (long-dashed curve) in the simulations at $z = 1$ before the gas removal. *Right:* Here, the ratio of total mass within a given radius at $z = 0$ over the total mass within a given radius before gas removal (at $z = 1$) is shown. The dotted (red) curve shows the gas removal simulation results, and the short-dashed (blue) curve gives the predictions of the adiabatic expansion model. The model gives 10 per cent accuracy for radii $r > 500$ pc and underpredicts the effect at smaller distances.

fraction of mass removed is $M_{\text{gas}}/M_{\text{tot}} = 0.09$. It is even smaller (0.02) inside the central 300 pc region. However, the final expansion was substantial. For example, the mass inside ~ 500 pc decreased by ~ 40 per cent.

The results of the cosmological hydro simulations, in agreement with results presented later from N -body simulations, show that the expansion of the halo takes place when a fraction of mass is removed from the central region. We approximated removal of the baryonic component of the hydro simulations in two ways. In our first trial, we removed the fraction of gas mass within a given radius from the dwarf's total mass and implemented the Blumenthal et al. (1986) expansion. This fraction varies with radius and produced weak expansion at small radii, as there was little gas mass within central ~ 1 kpc. In our second trial, we removed a constant mass fraction of 10 per cent at all radii, which corresponded to the average baryonic mass lost within the entire dwarf. Our second method, using constant removal, produced results in better agreement with the no gas hydro simulation.

In this case, the Blumenthal et al. (1986) prescription (equations 4 and 5) underestimated the expansion in the very centre but gave reasonably accurate results for radii larger than ~ 0.5 kpc. Constant mass removal is also more in line with the Gnedin et al. (2004) model. They found that expansion corresponds to more mass removed within a given radius than the expected value, after accounting for non-circular motions. The analytical model has the advantage that it can be used for different parameters and different configurations, so we use it to investigate the effects for different amounts of mass removal.

We consider a simple but realistic model in which baryonic effects cause the initial halo to retain a constant fraction of its density at every radius: $\alpha = \alpha_0 = \text{const}$. In this case, adiabatic expansion of the halo preserves the shape of the density distribution, but with modifications to its parameters. Any halo profile can be written in the form

$$\rho(r) = \rho_0 \Psi\left(\frac{r}{r_0}\right), \quad (6)$$

where r_0 is a scale radius and ρ_0 defines overall normalisation of the profile. The dimensionless function $\Psi(x)$ describes the density profile. For example, for the NFW profile (equations 1 and 2) one can choose $r_0 = r_s$ and $\Psi = 1/x(1+x)^2$. When the halo loses $1 - \alpha_0$ of its mass, it expands and changes the parameters r_0 and ρ_0 , but the function Ψ is preserved. Using equations (4)–(6) and labelling variables with the subscripts i for initial and f for final parameters, we get

$$\rho_{0,f} = \alpha_0^4 \rho_{0,i}, \quad r_{0,f} = \frac{r_{0,i}}{\alpha_0}. \quad (7)$$

Note the large power of α_0 in the equation for density normalisation. It means that the overall normalisation for the density declines very substantially. If we assume that most of the baryons were removed when a dIrr galaxy transforms into a dSph, then $\alpha_0 \approx 1 - f_b \approx 0.8$, which leads to a drop in density of $\rho_{0,f}/\rho_{0,i} \approx 0.4$. Next, we pose the question of how much the density changes at a given physical radius after baryon removal. The answer depends on the particular form of the density profile:

$$\frac{\rho_f(r)}{\rho_i(r)} = \alpha_0^4 \frac{\Psi\left(\frac{r}{r_{0,f}}\right)}{\Psi\left(\frac{r}{\alpha_0 r_{0,i}}\right)}. \quad (8)$$

If the function Ψ is the power law $\Psi \propto x^{-\beta}$, then

$$\frac{\rho_f(r)}{\rho_i(r)} = \alpha_0^{4-\beta}. \quad (9)$$

For the NFW profile, the central cusp has a slope of $\beta = 1$ and the density declines by large factor, $\rho_f/\rho_i = \alpha_0^3 \approx 0.5$, again assuming that $\alpha_0 \approx 0.8$. The change in the outer region is much smaller as $\beta = 3$, so $\rho_f/\rho_i = \alpha_0 \approx 0.8$. It is interesting to note that a density profile with a central core ($\beta = 0$) experiences the largest decline in density, $\rho_f/\rho_i = \alpha_0^4$.

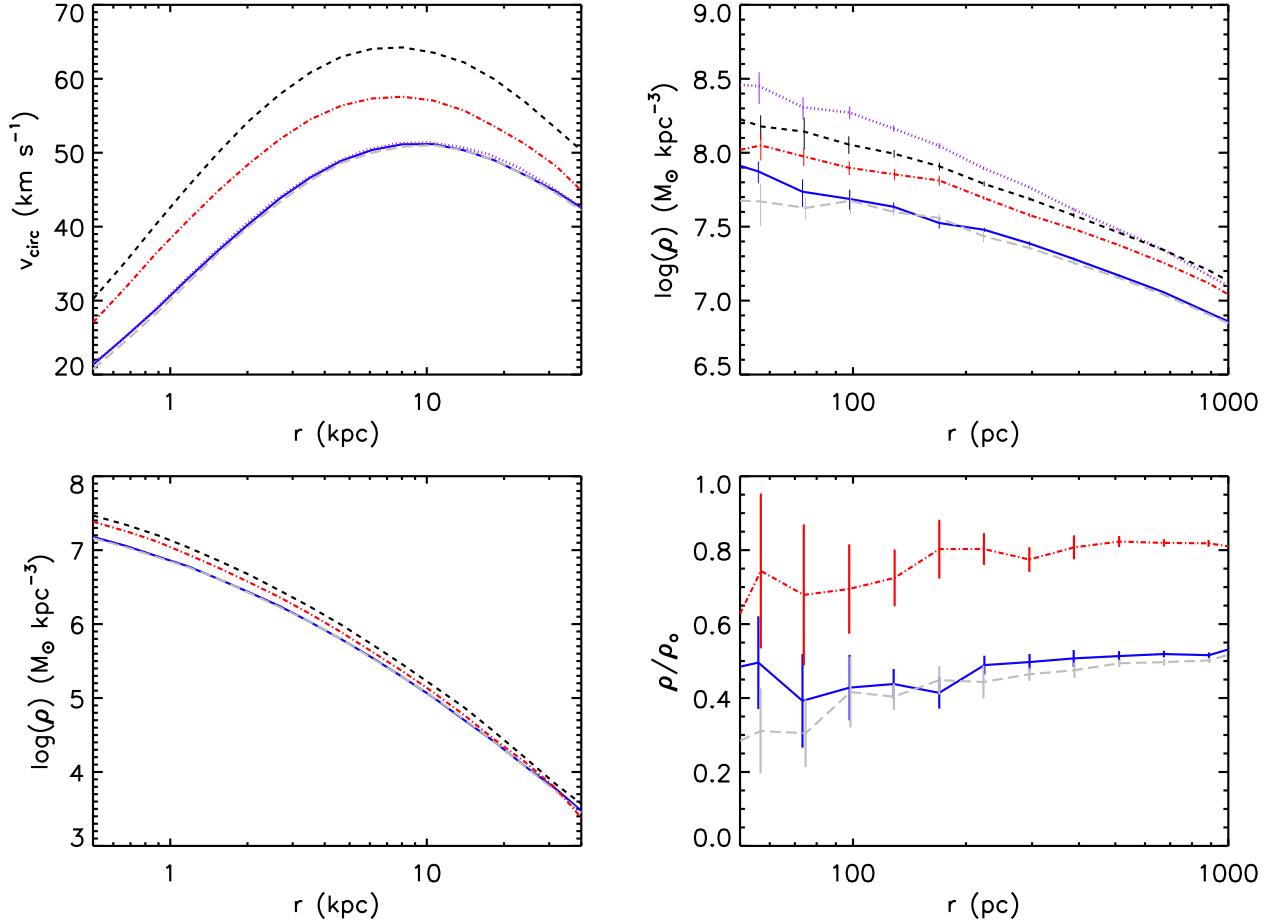


Figure 2. Profiles of dwarf galaxies at their final moment in isolated evolution. In all plots, the short-dashed (black) line shows the no mass removal case (NR), the dash-dotted (red) line shows the mass removal before the halo formed (PR), the solid (blue) line shows the exponential removal case (ER) and the long-dashed (grey) line shows the instantaneous removal case (IR). *Top Left:* The circular velocity profiles of the four dwarf galaxies. An additional line, dotted (purple), displays the adiabatic expansion model that the NR halo would incur if it lost 20 per cent of its mass. It lies on top of the ER and IR profiles, indicating they underwent adiabatic expansion. *Bottom Left:* The density profiles of all four dwarfs over the same range as above. *Top Right:* The density profiles of all four dwarfs, zoomed into the central 50 pc to 1 kpc region. The initial state of the dwarf, before any isolated evolution or mass removal, is included as the dotted (purple) line. The NR halo begins to deviate from this profile at 500 pc. *Bottom Right:* The fractional deviation in density of the mass removal cases divided by the NR profile. The profiles in the right two panels represent the mean of 21 profiles in order to reduce shot noise. The errors displayed are the associated errors in the mean.

4.2 Baryon removal in N -body simulations

The correct ratio of baryons to dark matter is important for an accurate representation of the structure of dwarf galaxies. Dwarf spheroidals are known for their high mass to light ratios, producing distributions that do not follow the cosmic mass fractions. In order to mimic this lack of baryons inside of Sphs, we removed some fraction of mass from our dwarfs. The mass removed should reflect the amount of baryonic matter lost when accounting for the lack of gas in dSphs. This left the DM mass of the galaxy unchanged. As the details of removal process are still unknown, we simply removed some fraction of the mass from our test dwarf in isolation to create a comparison between dwarfs from pure DM simulations with NFW profiles and those with baryons included.

To test a few cases, we have run four dwarfs in isolation under different conditions (see Table 2 for naming conventions). Our test dwarf (no mass removal – NR) was run for 1 Gyr from a equilibrium setup and is used as a benchmark for our comparisons to other dwarfs.

The three remaining dwarfs were modified using techniques that test a variety of ways a dwarf galaxy may have its baryonic component removed. On one extreme, we present the case where the majority of baryons have never entered the dark matter halo. Here, the dwarf will always be in equilibrium with the correct mass fraction, and there is no need to expel more baryons. This creates a steep inner density profile making mass removal via tidal stripping difficult. We explore this scenario with a dwarf that undergoes pre-halo formation mass removal (PR). It was evolved in isolation with an initial mass at 80 per cent of the no mass removal case and remained in equilibrium.

However, it is more likely that the dwarf once contained a baryonic component that was either expelled via SNe feedback, galactic winds, and radiation pressure or removed by ram pressure and tidal stripping. One dwarf (instantaneous removal – IR) began as the no removal case and then had 20 per cent of its mass instantaneously removed before evolving in isolation.

Another dwarf (exponential removal – ER) explored slow mass removal throughout its evolution in isolation. The mass be-

gan at the no removal level and then was reduced via an exponential function of the form: $m_i(t) = m_{i,0}(B + Ae^{-t/t_0})$. Each particle began with a mass of $m_{i,0}$ and currently has a mass of $m_i(t)$. We have implemented $t_0 \sim 200$ Myrs with $B = 0.8$ and $A = 0.2$. This equation allowed 20 per cent of the mass of each particle to be removed over an exponential time-scale, t_0 . The larger the value of the time-scale, the slower mass is removed. The removal time-scale should be larger than the dynamical time of the central region. Using $t_{\text{dyn}} = R/v_{\text{circ}}$ we found $t_{\text{dyn}} \sim 23$ Myrs for $R = 1$ kpc and $v_{\text{circ}} = 43 \text{ km s}^{-1}$ and $t_{\text{dyn}} \sim 16$ Myrs for $R = 0.5$ kpc and $v_{\text{circ}} = 30 \text{ km s}^{-1}$. It is apparent that the exact value depends on the definition of the inner region. Our choice of time-scale, $t_0 \sim 200$ Myrs, is an order of magnitude larger than these calculations.

In both the IR and ER cases, the galaxy initially had the same mass as the no mass removal case. When the baryons are removed, the halo is expected to adjust to the mass loss according to adiabatic expansion. The PR case examines how a dwarf of the same mass without expansion evolves. This tests the differences between haloes that undergo baryon removal with and without expansion.

4.2.1 Effects of fast and slow loss of baryons

The change in maximum circular velocity, v_{max} , throughout each dwarf galaxy's isolated evolution is given in Table 2. For the no mass removal case (NR), the initial v_{max} in the table is from the equilibrium conditions given by the code before any isolated evolution, and the final v_{max} is after isolated evolution. This shows how much the initial profile we provide relaxed after 10 dynamical times. For all other cases, the initial v_{max} listed is the final state of the NR case to show the deviation from the preferred equilibrium state of the dwarf galaxy.

Fig. 2 shows the density and circular velocity profiles of the dwarfs at their final moment of isolated evolution. We see that the removal of baryons after the halo has formed, via instantaneous mass removal (IR) or exponential mass removal (ER), dramatically reduced the circular velocity profile. Mass removal caused the halo to adiabatically expand, which reduced v_{max} and increased r_{max} , the radius where the velocity peaks. This can be seen in the difference between the NR halo and the ER and IR haloes. Our adiabatic expansion model, explained in Section 3.3, is also plotted as a circular velocity profile in Fig. 2. It began with the initial mass profile of the NR halo and used an $\alpha = 0.8$ to reduce the v_{max} and increase r_{max} . We find that our simple adiabatic expansion model reproduces the final circular velocity profiles of the ER and IR haloes very well.

In contrast, the removal of baryons before the halo has formed, as done in the PR case, caused v_{max} to decrease without an increase in r_{max} . This is because the halo did not undergo adiabatic expansion, as there is no baryonic removal from the halo, but instead the baryons were prevented from ever falling into the halo. This created a higher central density profile with a more pronounced cusp than in the adiabatic expansion cases.

The density profiles of the four dwarfs are also shown, with the largest difference between the simulations located in the central 1 kpc. To better examine the central density of the dwarfs, the right two plots in Fig. 2 zoom into the inner 50 pc to 1 kpc region. The upper right plot in Fig. 2 shows inner density profiles and includes the original NFW halo without mass removal and before relaxation. The NR density profile has relaxed for 1 Gyr, and differences between the initial NFW halo and the NR halo are only seen within

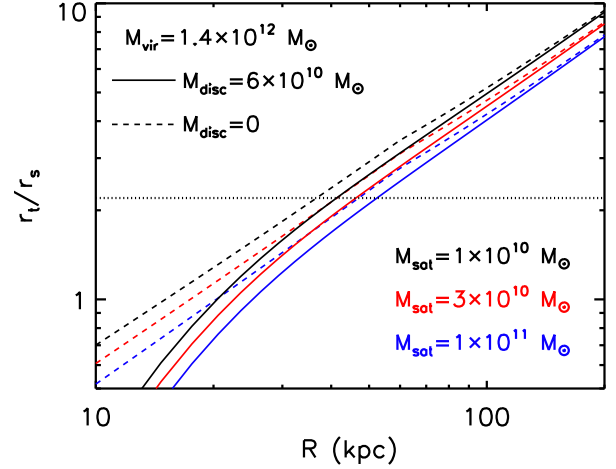


Figure 3. Dependence of the satellite truncation radius (in units of the scale radius) on the radial distance from the centre of its host halo. Satellites of varying masses ($M_{\text{sat}} = 10^{10}, 3 \times 10^{10}$, and $10^{11} M_{\odot}$) are shown from top to bottom and in black, red, and blue, respectively. Dashed lines show the truncation radii for satellites orbiting in the presence of a pure NFW halo ($M_{\text{vir}} = 1.4 \times 10^{12} M_{\odot}$) as contrasted with solid lines of the same colour showing a primary halo that also contains baryons ($M_{\text{disc}} = 6 \times 10^{10} M_{\odot}$) that coalesced at the centre of the halo. The horizontal dotted line denotes $r_t = 2.2r_s$. The internal structure of subhaloes can be dramatically affected when their orbits include pericentric passages with truncation radii below $2.2r_s$.

the inner 500 pc. We compare all isolated dwarf cases to the NR case, as it represents the preferred equilibrium state of the dwarf.

The lower right panel of Fig. 2 shows the density of the three mass removal cases divided by the NR case. Here, we examine how the density ratio differs for different mass removal cases and how this compares to a DM only dwarf. Both the IR and ER cases evolved to have similar fractional density profiles with only half the original halo's density in the central region. The halo that never allowed baryonic infall (PR) retained 0.8 of the NR density profile. All profiles remained fairly flat without a large central density deficit. A decrease would have indicated the creation of a core from the traditional cuspy interior of the NFW profile. However, we do not see this effect occurring as a result of mass removal with or without adiabatic expansion.

The PR case will examine how tidal stripping impacts a satellite that does not experience expansion. The IR and ER cases explore the combined effects of expansion and tidal stripping for a massive dwarf. We expect that the IR and ER cases will be more susceptible to tidal stripping than the PR case as they have experienced an increase in r_{max} .

5 EFFECTS OF TIDAL STRIPPING

5.1 Truncation radius: analytical estimates

In order to examine how the concentration of baryons in the inner part of the MW halo impacts the subhalo, we begin by presenting analytical estimates of the subhalo's tidal radius, depending on its mass, the main halo mass, its distance from the main halo, and the inclusion or absence of baryons in the centre of the primary. One needs to be aware that the fate of the dwarf strongly depends on the tidal radius, r_t , to which it is stripped. We later show that if $r_t > 4r_s$, there is no significant evolution of v_{max} . However, tidal

stripping can even alter the very centre of the dwarf when $r_t < 2r_s \sim r_{\max}$. So there is a transition at $r_t \sim 2r_s$ with a small effect for larger r_t and drastic stripping at smaller tidal radii.

If the subhalo has a mass profile of $m(r)$, which orbits a halo with mass profile $M(R)$ at a radius R , then the tidal radius for the subhalo, r_{tide} , is defined as the radius of the subhalo at which the gravitational force on a test particle from the subhalo equals the difference of the gravitational force (tidal force) from the halo on the subhalo and the test particle (see e.g. Klypin et al. 1999a),

$$G \frac{m(r_{\text{tide}})}{r_{\text{tide}}^2} = -\frac{\partial}{\partial R} \left[\frac{GM(R)}{R^2} \right] r_{\text{tide}}. \quad (10)$$

$$\frac{m(r_{\text{tide}})}{r_{\text{tide}}^3} = \frac{M(R)}{R^3} \left[2 - \frac{R}{M} \frac{\partial M}{\partial R} \right]. \quad (11)$$

The subhalo can also be stripped to an even smaller radius defined by resonances between the gravitational force from the subhalo and the tidal force from the halo. This resonant radius can be obtained by solving the following equation:

$$\frac{m(r_{\text{res}})}{r_{\text{res}}^3} = \frac{M(R)}{R^3}. \quad (12)$$

The smaller of r_{tide} and r_{res} is taken as the truncation radius. This is denoted by r_t and defined as the radius to which the subhalo is stripped.

For haloes following the NFW density profile, the mass profile $m(r)$ is given by

$$m(r) = M_{\text{vir}} \frac{\mu(x)}{\mu(c_{\text{vir}})}, \quad x \equiv \frac{r}{r_s}, \quad (13)$$

where r_s is the scale radius of the halo and is related to the virial radius of the halo through the concentration parameter, $c_{\text{vir}} = r_{\text{vir}}/r_s$, and the function $\mu(x)$ is given by equation (2). We assume that the subhalo mass profile follows the above distribution.

The main halo includes a dark matter component that follows the NFW profile and a baryonic component that is concentrated at the centre of the halo and is well inside the orbit of the satellite. Therefore, the total mass profile of the halo is given by

$$M(R) = M_{\text{bar}} + M_{\text{vir}}(1 - f_b) \frac{\mu(x)}{\mu(c_{\text{vir}})}, \quad (14)$$

where $x = R/R_{\text{vir}}$ and C_{vir} is the concentration of the halo. The parameter f_b is the fraction of the virial mass that is in the baryonic component: $f_b = \Omega_{\text{bar}}/\Omega_{\text{matter}}$. Here, Ω_{bar} and Ω_{matter} are the contributions of the baryons and the total matter as compared to the critical density of the Universe, respectively. We assume that the baryonic mass of the halo is $M_{\text{bar}} = 6 \times 10^{10} M_{\odot}$, consistent with the baryonic mass estimates for the MW (e.g., Dehnen & Binney 1998; Klypin, Zhao, & Somerville 2002).

To determine the truncation radius, r_t , we substitute the mass profiles for the subhalo (equation 13) and the main halo (equation 14) into the tidal and resonant radii equations (11) and (12). A range of subhalo masses and virial host masses are used to examine how the mass of both the primary and secondary impacts tidal stripping.

The results of these calculations are in Fig. 3, which depicts the dependence of the satellite truncation radius (in units of the scale radius) on the radial distance from the centre of its host halo. Decreasing values of r_t/r_s indicate more tidal stripping because, as the tidal radius approaches the scale radius of the satellite, an increasing amount of mass is stripped. The maximum circular velocity occurs at a scale radius $r_s = 2.2$; so when $r_t/r_s \sim 2$, internal structure is affected. Satellites of varying masses are shown with

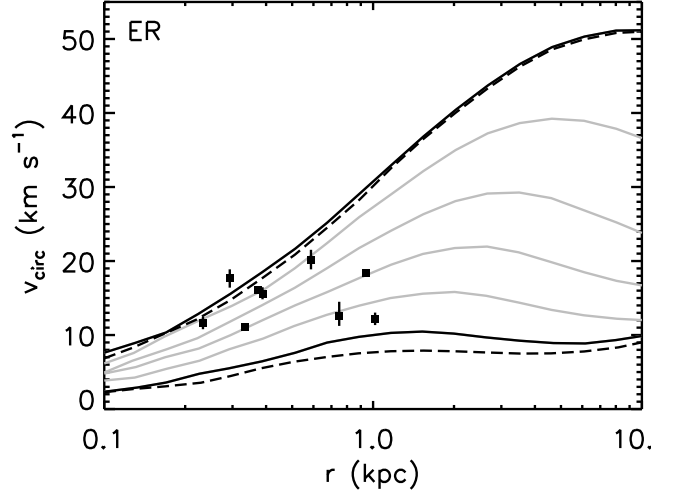


Figure 4. Evolution of the circular velocity profiles for two mass removal satellites after experiencing 50 kpc circular orbits. The exponential mass removal (ER) satellite is shown in solid lines. The upper and lower black lines indicate its initial and final states, respectively, while the grey lines in between are each separated by one Gyr. After 5 Gyrs, the satellite's v_{max} has been stripped from 50 to 10 km s^{-1} . The initial and final state of the instantaneous mass removal (IR) case is shown as dashed (black) lines for comparison. The black squares are observational data points of the half-light velocities for the classical Local Group dSphs.

different colours. Smaller haloes collapse earlier, increasing their concentration. This results in a larger density at r_s , causing the less massive satellites to be more resilient against tidal stripping.

Fig. 3 includes results from a NFW main halo ($M_{\text{vir}} = 1.4 \times 10^{12} M_{\odot}$) with and without a fraction of the baryons ($M_{\text{disc}} = 6 \times 10^{10} M_{\odot}$) coalesced at the centre. The pure-NFW halo mimics cosmological simulations, where baryons are assumed to trace the dark matter in an unbiased way. The impact of including a disc component is clearly seen for orbits with pericentres within ~ 30 kpc. At this radius, each satellite's tidal radius decreases by ~ 14 per cent, which is a significant effect. For orbits with pericentres within ~ 20 kpc, the satellites will be destroyed under the influence of a MW with or without a disc component because $r_t/r_s \lesssim 1$. In contrast, if the pericentre is greater than 100 kpc, then $r_t/r_s > 4$ regardless of whether a disc component is included or not, which produces weak tidal stripping.

For the regime of orbits with $30 \text{ kpc} \lesssim r \lesssim 100 \text{ kpc}$, the inclusion of a disc has a more subtle but important effect. From $30 \text{ kpc} \lesssim r \lesssim 60 \text{ kpc}$ the satellites have obviously strong tidal stripping if the MW disc is included. Orbits with $60 \text{ kpc} \lesssim r \lesssim 100 \text{ kpc}$ may also undergo increased tidal stripping and should be examined further. We predict that the inclusion of a disc for orbits with these pericentres results in an important regime of mass loss and circular velocity decrease. As such, we have created satellites on elliptical orbits with pericentres between 30 kpc and 70 kpc, to investigate this region.

5.2 Effects of tidal stripping in N -body simulations

Each of our three dwarf galaxy mass removal cases had 20 per cent of its mass removed, but they produced different maximum circular velocity values and central density profiles. Instantaneous mass removal (IR) and exponential mass removal (ER) scenarios both resulted in a 20 per cent reduction in v_{max} due to adiabatic expan-

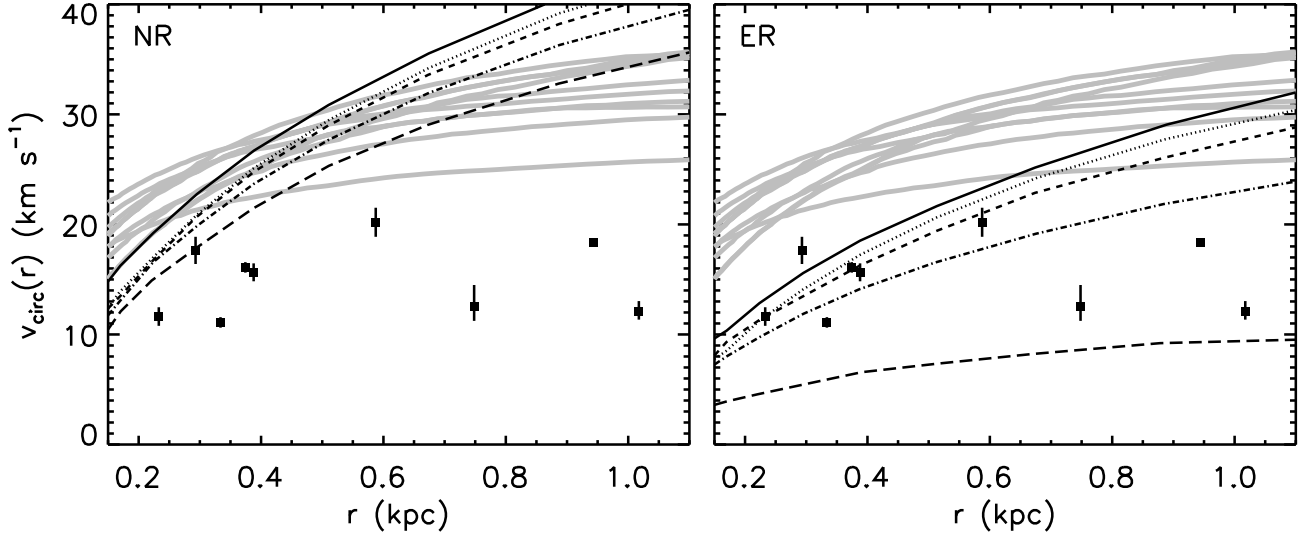


Figure 5. Comparison of our circular orbits to observations of the MW satellites (black squares) and the Aquarius E halo’s “massive failures” from the analysis of Boylan-Kolchin et al. (2012) (thick grey lines). *Left:* The circular velocity profiles of the no mass removal case (NR). This profile does not agree with the MW dSph population and was created to mimic the Aquarius cosmological simulations. *Right:* The circular velocity profiles of the exponential mass removal case (ER). These profiles span a much larger range of parameter space and are in agreement with observed MW dwarfs due to their inclusion of baryonic effects. Both panels show the initial isolated profile as a solid black line. The circular orbits after 5 Gyrs of evolution are shown from top to bottom as: 150 kpc (dotted), 100 kpc (short-dashed), 70 kpc (dash-dotted), and 50 kpc (long-dashed).

sion. The pre-halo formation mass removal scenario (PR) did not undergo adiabatic expansion; therefore, its v_{\max} only decreased by 10 per cent in isolation. See Section 4.2 for the mass removal description and results.

After each dwarf evolved in isolation, they were put into a variety of circular and elliptical orbits around a MW-like host as described in Section 3.2.3 and listed in Table 3. Comparing the orbital evolution of these three haloes will provide insight into how pericentre passage, number of orbits completed, and central density of the satellite impacts the final maximum circular velocity values.

5.2.1 Circular orbits

Four different dwarfs were placed in circular orbits around the MW perturber. The no mass removal dwarf (NR), which had evolved in isolation, was placed around a pure-NFW perturber to mimic the results of DM only simulations. The three mass removal dwarfs – two that showed adiabatic expansion (IR and ER) and one without (PR) – were placed in circular orbits around a MW perturber with a NFW and spheroidal exponential “disc” component. All satellites were simulated for 5 Gyrs with initial and final maximum circular velocities listed in Table 3.

We investigated two regimes (i) at $r \geq 100$ kpc where the mass loss was expected to be low based on our truncation radius analysis ($r_t/r_s > 4$) and (ii) at $30 \text{ kpc} < r < 100$ kpc where the truncation radius ratio had values between $2 < r_t/r_s < 5$. This second regime is a sensitive area where a large amount of mass may be lost if the tidal radius becomes small enough. For pericentre passages within 30 kpc, $r_t/r_s < 2$ resulting in extreme tidal stripping for the satellite regardless of its mass or central density.

To investigate the first regime, two different circular orbits were created. One was created at 150 kpc and another was created at 100 kpc. The truncation radius to scale radius ratio (r_t/r_s) is large at this orbital distance (for NR with a pure NFW MW: $r_t/r_s = 8.7$ at 150 kpc and $r_t/r_s = 6.3$ at 100 kpc). Due to the

large ratio, very little matter would be stripped from the satellite even after a long time period in a stable orbit. This was confirmed by the results quoted in Table 3, where the 150 kpc orbits for the NR case showed a 5 per cent change in the satellite’s v_{\max} . The mass removal case without adiabatic expansion (PR) showed a 7 per cent change.

Even in distant orbits, the combined effects of including baryons in simulations, namely mass removal with subsequent adiabatic expansion and the inclusion of a baryonic disc, doubled the reduction in v_{\max} from 5 to 10 per cent (for 150 kpc orbit) and 11 to 22 per cent (for 100 kpc orbit), as given in Table 3. Mass loss was even more significant than the change in v_{\max} , with losses of 60 per cent in a 150 kpc orbit and 80 per cent in a 100 kpc orbit for the ER case. This shows that the evolutionary history of galaxies in pure DM simulations may produce incorrect masses of subhaloes at redshift zero, even if they do not interact closely with their hosts.

Closer circular orbits at 70 and 50 kpc were run to examine more extreme tidal stripping. Although the haloes had different r_t/r_s values, all underwent significant mass loss after 5 Gyrs. The most dramatic of these were the ER and IR 50 kpc orbits. Fig. 4 displays the significant tidal stripping satellites experience when orbiting close to their host, by examining their circular velocity profiles. The ER case is shown every Gyr throughout its 50 kpc circular orbit, and the initial and final IR profiles are shown for comparison. This allows one to trace the evolution of the entire circular velocity profile for this specific case.

The v_{\max} and r_{\max} of the ER case decreased with time until the final satellite has $v_{\max} = 10 \text{ km s}^{-1}$, with a significant fraction of bound mass existing as tidal arms and tails. At 2 Gyrs, the v_{\max} has decreased by 40 per cent, converting a 51 km s^{-1} subhalo to a much smaller 30 km s^{-1} satellite. The initial and final IR velocity profiles are also shown in Fig. 4 for comparison. Although the ER and IR cases began with similar circular velocity and density profiles, the final IR case is slightly more disrupted than the ER subhalo, which retained a small satellite core.

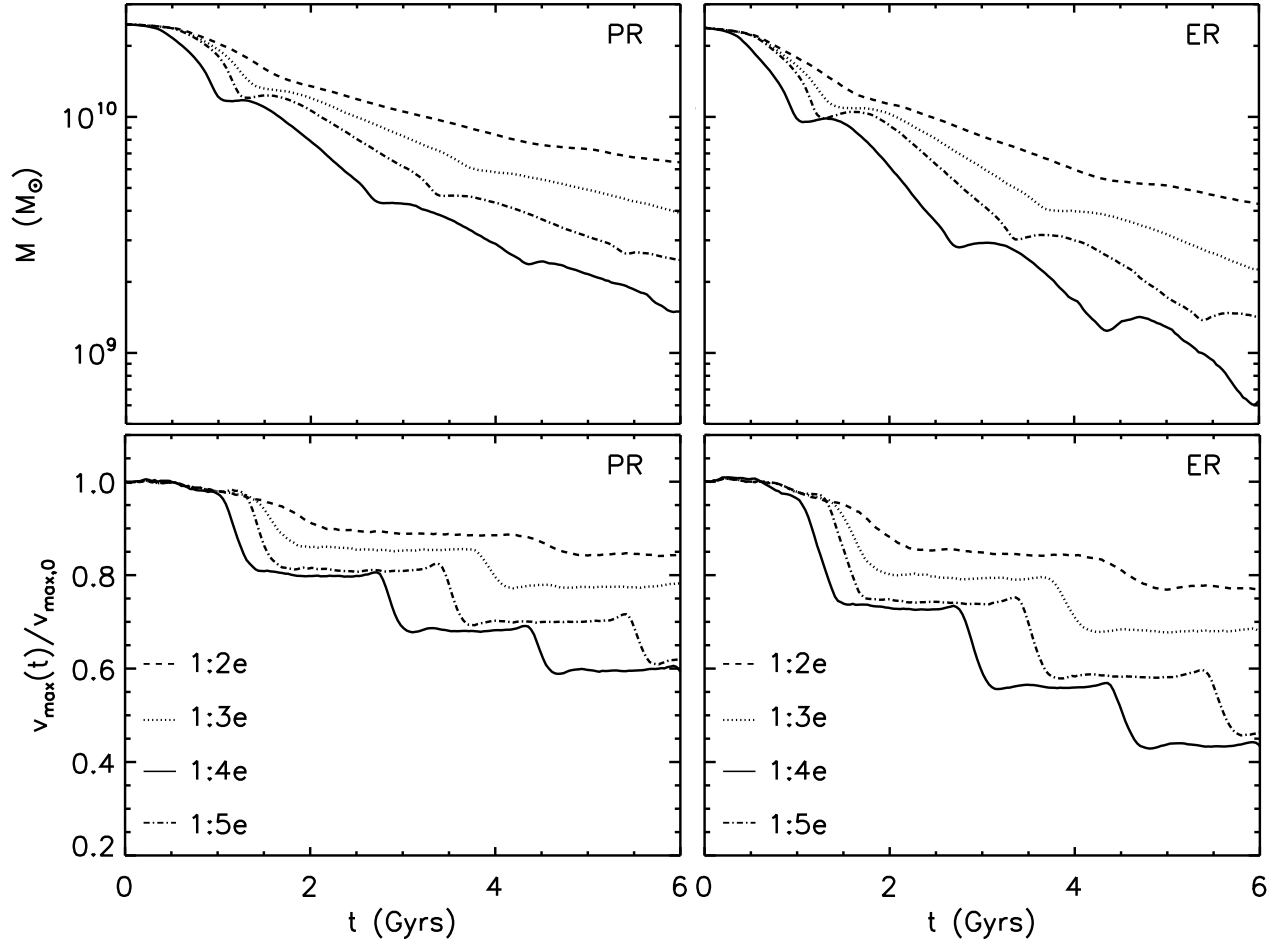


Figure 6. Mass evolution and fractional change in maximum circular velocity ($v_{\max}/v_{\max,i}$) for the pre-halo removal (PR), which is on the left, and exponential removal (ER) satellite, which is on the right. The four elliptical orbits: 1:2e (150 kpc to 70 kpc), 1:3e (150 kpc to 50 kpc), 1:4e (120 kpc to 30 kpc), and 1:5e (150 kpc to 30 kpc) are shown. Mass continually decreases throughout the 6 Gyrs of evolution. Pericentre passages occur at the steep drops in both mass and v_{\max} . The 1:4e and 1:5e orbits have the same pericentre distance of 30 kpc, with the difference being their apocentres. The 1:5e orbit experiences less mass and v_{\max} loss at a given time because of the longer time to complete one orbit. If this time-scale is taken into account, the same pericentre distances create very similar evolutionary histories.

Observational data points of the half-light velocities for the classical Local Group dSphs are shown in Fig. 4 as well. The initial ER profile is too massive to be consistent with the majority of Local Group dSphs but is consistent at 2σ with Draco, the data point just above it, and Leo II, the data point with the smallest radius value. After 1 Gyr of evolution, the ER subhalo is consistent with four observational data points, and after 3 Gyrs, two more observations match the ER satellite’s circular velocity profile. At the end of 5 Gyrs of evolution, the satellite is capable of matching all observed Local Group dSphs at some point in its evolutionary history. The gravitational effects due to the expulsion of baryons have converted a massive satellite, incapable of matching any of the Local Group dSphs, into a dwarf that matches a given observed dSph at a fixed time in its evolution.

The ER and IR satellites have a $r_t/r_s = 2.2$ for the 50 kpc orbit. As seen in the evolution of the circular velocity profiles, satellites with this low tidal to scale length value are capable of undergoing extreme disruption and possibly becoming completely destroyed. It is within the $2 < r_t/r_s < 4$ region that tidal stripping may become significant depending on pericentre passage, number

of orbits completed, and central density of the satellite. This will be further examined in our elliptical orbits.

As a comparison between the satellites run in circular orbits, Fig. 5 shows the circular velocity profiles of the NR (left panel) and the ER cases (right panel). This figure also includes observational data points of the half-light velocities for the classical Local Group dSphs and lines from Boylan-Kolchin et al. (2012) Fig. 3 for the Aquarius E halo. We plot both the isolated NR and ER haloes over these data and the results of the 150 kpc, 100 kpc, 70 kpc, and 50 kpc circular orbits at 5 Gyrs.

The initial NR subhalo was created in order to match cosmological simulations, without baryon removal and without a MW disc component. The circular velocity profile for the NR halo is consistent with the Aquarius satellites in that it does not match any of the observed MW satellites. The initial ER satellite is in better agreement because it includes mass removal even before it evolves on a circular orbit. This demonstrates how baryonic removal alone brings the subhaloes into agreement with MW satellites. Creating an initial NR dwarf with a more typical, low total mass value, would provide even better agreement between the initial ER dwarf and observed subhaloes.

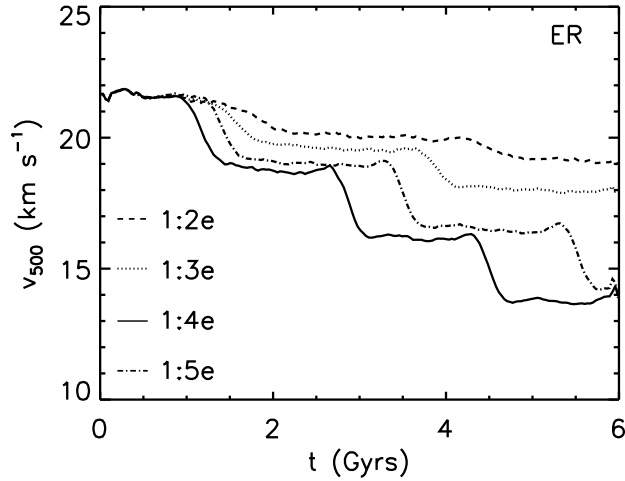


Figure 7. Shown is the evolution of circular velocity at 500 pc for the exponential removal (ER) case. Each elliptical orbit (1:2e, 1:3e, 1:4e, and 1:5e) is shown with a different linestyle. The velocity at this set radius decreases dramatically as the satellite approaches pericentre, similar to how v_{\max} evolved in Fig. 6.

After undergoing circular orbits for 5 Gyrs, the NR halo remained inconsistent with observations for the 150 kpc, 100 kpc, and 70 kpc orbits. This is in agreement with the results of Boylan-Kolchin et al. (2012), who found many subhaloes that were too dense and had circular velocities that were too large to match the MW satellite population. Only with an extremely close circular orbit (50 kpc), does the NR satellites agree with Draco.

The ER satellite included both mass removal and a MW disc component. The results for this halo are in much better agreement with the entire population of Local Group dSphs. As seen in Fig. 5, the 100 kpc orbit is in agreement with four of the observed dSphs. When the satellite is placed in a circular orbit with a 50 to 70 kpc radius, it is able to match the four dSphs with the smallest circular velocity profiles. The importance of including the MW disc is seen from these orbits as significant tidal stripping reduces their mass and maximum circular velocity values.

5.2.2 Elliptical orbits

Results from our circular orbits motivated us to create elliptical orbits that have pericentres within the interesting range of truncation radii from $1 < r_t/r_s < 5$. Our range in dwarf masses, in combination with a desire to create realistic ellipticities and pericentres, resulted in four orbits with apocentre–pericentres of 150–70 kpc, 150–50 kpc, 120–30 kpc, and 150–30 kpc.

As the satellites began their orbits, they immediately started to lose mass under the tidal influence of the MW. At their first pericentre passage, most had already lost over half their mass. The second orbit continued to induce strong mass loss, and by their second pericentre passage, some satellites had only one fifth of their mass remaining. Both the mass and maximum circular velocity evolution for the PR and ER satellites over 6 Gyrs are shown in Fig. 6 for all different orbits. The maximum circular velocity plot is shown as a fraction of the original maximum circular velocity value, while the mass is plotted in solar masses.

Each “step” in the circular velocity plot marks a pericentre passage, which also aligns with the “bounce” or change in slope of the mass evolution. However, mass is lost continuously through-

out the orbit, as opposed to v_{\max} , which only changes significantly at pericentre passage. For the most distant orbit (1:2e), the mass shows a smooth decrease, but the closer orbits have increased mass loss and change in circular velocity. At pericentre, the mass tends to increase slightly before decreasing once again. This is due to some of the mass in the tidal features temporarily becoming bound to the satellite. We found v_{\max} to be a more robust parameter for describing the transformation a satellite has undergone throughout its orbit.

Note that the 1:4e (120–30 kpc) and 1:5e (150–30 kpc) lines occur in reverse order on the plot, with 1:5e undergoing less mass and v_{\max} loss than the 1:4e case. Although this may seem strange at first glance, it is due to the pericentres and apocentres chosen for the orbits. The 1:2e, 1:3e, and 1:5e orbits all have apocentres of 150 kpc. However, the 1:4e orbit has an apocentre of 120 kpc and the same pericentre as the 1:5e orbit, resulting in a shorter orbital time-scale. This means the 1:5e orbit has less mass loss at any given time. What is most interesting is that after the same number of pericentre approaches, the change in mass and v_{\max} is approximately the same for the 1:4e and 1:5e orbits. This shows that the pericentre distances, and consequently the tidal radii, are good indicators of total tidal stripping.

A more accessible parameter for observers is a measurement of the circular velocity within the central region of the galaxy. To this effect, we provide the evolution of circular velocity at 500 pc in Fig. 7. Here, we see similar evolution as for v_{\max} but with final values in the range of 14 to 19 km s^{-1} .

When comparing the elliptical orbit profiles to the Local Group data points and the work of Boylan-Kolchin et al. (2012), as done in Fig. 5 with circular orbits, we find similar trends. The NR halo is not compatible with the Local Group dwarfs in elliptical orbits. The PR halo with 1:2e and 1:3e orbits are only consistent with Draco, and the 1:4e and 1:5e orbits are consistent with two additional Local Group dwarfs within 2σ .

The initial circular velocity profile of the PR halo was lower than the NR case but only matched the initial ER halo profile after a 1:4e orbit around the MW. We find that simply including a disc component in the MW is not sufficient to create agreement between our dwarf and the Local Group dSph population. Both the PR and ER haloes have the same total mass and evolve on the same orbits, providing evidence that the internal structure of the dwarfs drives the difference between their final profiles.

The ER halo is able to match all but the lowest two Local Group dwarfs with the elliptical orbits inducing significant tidal stripping. The results of the ER 1:2e and 1:3e orbits are similar in strength, lying between the 100 kpc and 70 kpc circular orbits, for the same halo. The 1:4e and 1:5e orbits are stronger than the 70 kpc circular orbit but not as dramatic as the 50 kpc orbit, with $v_{\text{circ}}(1.1 \text{ kpc}) = 20 \text{ km s}^{-1}$ for the 1:4e orbit. This agreement with the Local Group dwarfs once again shows the importance of including our two baryonic effects within simulations in order to match observations.

Next, we investigated how changing the ellipticity and pericentre distances affected mass removal, based on r_t/r_s . In Fig. 8 we show the fractional change in mass and v_{\max} after 5 Gyrs in relation to the r_t/r_s of each satellite. We calculated the truncation radius of our subhaloes at pericentre according to equations (11) and (12). Circular orbits have radii of 150 kpc, 100 kpc, 70 kpc, and 50 kpc, and elliptical orbits have pericentres of 70 kpc, 50 kpc, and 30 kpc.

To evaluate the truncation radii values, we input the analytic form (disc plus NFW) of the MW mass, $M(R)$, and pericentre dis-

tance, R , into equation (11). In order to obtain a correct value for r_t , no analytic form of the satellites' mass profile, $m(r)$, was used. Instead, numerical results from the isolated equilibrium haloes were input. The tidal radius, r_{tide} , was then solved for each satellite and pericentre combination. We also solved for the resonant radius using this method. The minimum of r_{res} and r_{tide} was taken as the truncation radius, r_t . This was divided by the satellites' r_s to create the value r_t/r_s .

Now that we have defined r_t/r_s for each satellite case with a different pericentre, we examined how the tidal radius impacts the mass loss after 5 Gyrs of evolution. In Fig. 8, we show satellite cases in different colours and symbols for different orbits, as listed within the figure. The instantaneous removal case is not included on this plot because the mass and v_{max} loss versus r_t/r_s values are almost identical to those seen in the exponential removal case.

It is apparent that for satellites with pericentres that are large enough to reach $r_t/r_s > 4$ the tidal stripping is minimal. As expected, over half of a satellite's mass is lost, but the v_{max} does not suffer a similar reduction. The fraction of v_{max} remains above 0.8 for these cases. For example, the shift in r_t/r_s between the NR 150c and ER 150c points is due to the adiabatic expansion of the mass removal haloes, which increases their r_s values. This gives smaller r_t/r_s values, while only slightly lowering their v_{max} fraction.

However, for satellites on orbits that reach $r_t/r_s \sim 4$ and below, there is a broad range of possible mass loss scenarios. In this regime, a satellite's mass can range from 0.3 to 0.05 times the original total mass, and the circular velocity can drop to 0.8 to 0.2 its original value. This is a dramatic decrease, indicating that tidal radius over scale radius at pericentre is an important parameter for predicting mass loss.

The r_t/r_s values of the PR haloes are significantly larger than those of the ER haloes, as denoted by different colours with the same symbols. The internal structure of the halo makes the PR cases resistant against tidal stripping so that the satellite does not experience as large a reduction in v_{max} or mass.

The separation between the circular and elliptical orbits is due to the length of time that the satellites sit near the primary. As circular orbits are always at the same distance, they are able to reduce their mass and v_{max} more, over 5 Gyrs of evolution, than an elliptical orbit with the same pericentre. Points with the same r_t/r_s value indicate that they have the same pericentre. This makes for an easy comparison between points that lie on vertical lines. For example, the 70 kpc circular orbit (70c) and the 150–70 kpc elliptical orbit (1:2e) have the same r_t/r_s for each satellite case of a single colour. The vertical separation between these pairs of points is due to the length of time they are close to the primary.

Although satellites on circular orbits undergo a larger number of orbits around the MW in the same amount of time as the elliptical orbits, the tidal forcing they feel is constant throughout all time. This means that tidal truncation is the main method of mass removal, without tidal shocks. We have included our tidal stripping model, as described in Section 3.4, that mimics tidal truncation. Unbound mass is iteratively removed from the satellite, and the tidal radius is recalculated with each iteration. The results of this model with 10 and 30 iterations are plotted in Fig. 8. Our simulation results typically fall between these two lines, indicating that the number of pericentre passages, as modelled by the number of iterations, can account for the spread between points with the same r_t/r_s value.

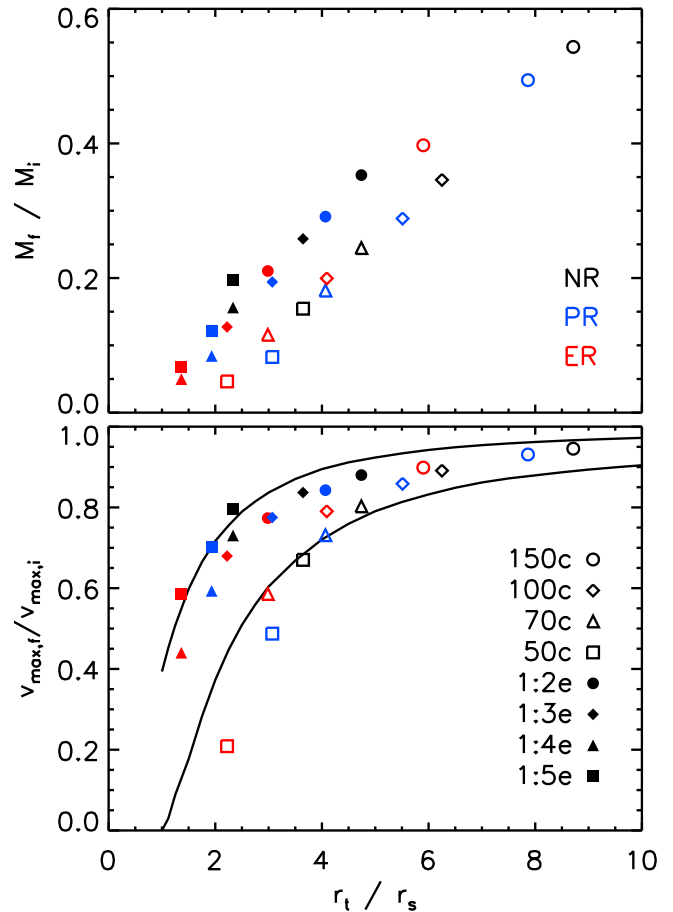


Figure 8. Results of tidal stripping for the mass and v_{max} of a satellite after 5 Gyrs. Symbols indicate different orbits with open symbols for circular orbits and filled symbols for elliptical orbits. The colours indicate different satellite cases: red is for exponential removal, blue is for pre-halo formation removal, and black is for no removal. Different satellite cases (colours) with the same orbit (symbol) always occur from left to right as ER, PR, and then NR, with increasing values of r_t/r_s . The fraction of mass retained increases linearly with increasing r_t/r_s so that the NR case always has the largest final mass fraction. When r_t/r_s is below 4, tidal stripping is very important, as seen by the significant mass loss and decrease in $v_{\text{max},f}/v_{\text{max},i}$. The solid black lines display our model for tidal stripping by iteratively removing all unbound particles and recalculating the tidal radius. The results of 10 and 30 iterations are the top and bottom solid lines, respectively.

6 CONCLUSIONS

One of the goals of this paper is to resolve some of the small-scale problems of the standard Λ CDM model, namely the apparent overabundance of satellites with $30 \text{ km s}^{-1} < v_{\text{circ}} < 50 \text{ km s}^{-1}$ (Boylan-Kolchin et al. 2011, 2012). In line with other recent results of cosmological simulations of galaxy formation (Zolotov et al. 2012; Brooks & Zolotov 2012; Brooks et al. 2012), we argue that the solution of the problem is in the gas physics of forming dwarf galaxies. By posing the question what are the effects of baryons on dwarf galaxies, we hope to examine just one aspect of the increasingly complicated fields of galaxy formation and evolution.

Most of the existing theoretical predictions and constraints on the abundance and structure of small satellites (“substructures”) are made using N -body simulations. Because observed dwarf galaxies in the MW are heavily dominated by the dark matter, one expects that there is little impact of baryonic physics on the structure of

dwarf satellites. However, this appears not to be true; the corrections due to baryons are significantly larger than one would naively expect.

Baryon removal may reduce the maximum circular velocities of satellites enough to explain the “too big to fail” problem. The central mass distribution of a dwarf may be substantially altered both by gas removal at infall and by tidal stripping due to the host galaxy. N -body simulations underestimate stripping because (i) baryons are not removed from the dwarf and (ii) the mass of the host is not enhanced by infalling baryons. Accounting for these effects can alter the circular velocity profiles of the subhaloes, such that they are “small enough to succeed” in explaining the observed structure of the Milky Way dSphs.

We used a number of methods to investigate how baryonic physics impacts the structure of a dwarf spheroidal. We ran hydrodynamical cosmological simulations, high resolution N -body simulations, and an adiabatic expansion model to examine the effects of baryon removal from dwarf galaxies. The impact of tidal stripping on dwarf galaxies was explored using a series of high resolution N -body simulations and two analytical models.

Our two high resolution cosmological simulations were run with and without gas removal. The gas removal case was created to reproduce the heating and removal of gas as a dIrr falls into a host galaxy. This dwarf expanded adiabatically in response to the mass loss. Baryon removal from the N -body simulations also resulted in adiabatic expansion for our exponential and instantaneous mass removal cases. The rate of removal of the gas does not affect the final results. In other words, both fast and slow removal provide the same amount of expansion.

The gas removal results were modelled with the Blumenthal et al. (1986) prescription for adiabatic expansion. Mass removal causes dwarfs to both expand and lower their circular velocities. The magnitude of the expansion depends on the fraction of mass removed and on the slope of the density. In the case when the same fraction of mass is removed independent of radius, the shape of the density profile does not change. The maximum decline in the density, according to adiabatic expansion model, is equal to $(1 - f_b)^4$, where f_b is the cosmological fraction of baryons. This decline is expected to happen for galaxies with constant density cores. For galaxies with cusps, the decline is smaller. For the NFW $\beta = -1$ cusp, the decline is still substantial with $\rho_f/\rho_i = (1 - f_b)^3$. If we assume that the mass removed is the cosmological average fraction, then $\rho_f/\rho_i \approx 0.5$.

We tested a series of circular and elliptical orbits for each dwarf with high resolution N -body simulations. Without baryon removal, tidal stripping during an orbit around a pure-NFW host creates profiles similar to the Boylan-Kolchin et al. (2012) results. Our no mass removal dwarf does not agree with the half-light velocities of the Local Group dSph population after 5 Gyrs of evolution in circular or elliptical orbits.

The combination of tidal evolution around a MW with both a NFW and disc component and baryonic removal with adiabatic expansion was tested with the exponential and instantaneous mass removal dwarfs. Both experienced large amounts of mass removal and a significant reduction in v_{\max} . This brought them into agreement with every Local Group dSph over the course of at least one of the elliptical or circular orbits.

Tidal evolution alone was also examined in our pre-halo formation mass removal dwarf. This subhalo had the same mass as our other baryon removal cases but without adiabatic expansion. It experienced weaker tidal stripping due to its steep inner density profile, making it compatible only with the five most massive Lo-

cal Group dSph population after evolution in elliptical and circular orbits.

In order to quantify how the inner regions of the dwarf are impacted due to tidal stripping, we created two analytical models. The first calculated how a dwarf’s tidal radius changes depending on the mass of the dwarf, the mass of the primary, the distance from the main halo, and the inclusion or absence of baryons in the central region of the host. We found that r_t/r_s , the tidal radius over the scale radius of the satellite, is able to predict the strength of tidal stripping. When r_t/r_s is greater than 4, there is no significant evolution in v_{\max} . However, when r_t/r_s is less than two, the central region of the dwarf is subject to tidal forces and may be significantly altered.

The second analytical model for tidal stripping iteratively removed unbound particles, estimated the correct adiabatic expansion the halo would undergo from this amount of removal, and then recalculated the tidal radius. This model was able to reproduce our N -body simulations in the context of reduction in v_{\max} and mass as a function of r_t/r_s and time in orbit. We find that each iteration continues to remove some fraction of the particles without convergence on a value.

Our main conclusions are as follows:

- (i) Our simulations show that without baryon removal or tidal stripping, dwarfs match the results from the Boylan-Kolchin et al. (2012) analysis of the Aquarius simulations.
- (ii) Baryon removal with adiabatic expansion is very effective, bringing initially extremely massive dwarfs into agreement with observations before any orbital evolution.
- (iii) Including the effects of tidal stripping without expansion due to baryon removal is insufficient to reproduce the entire observed dSph population for the case of an initially massive dwarf.
- (iv) The inclusion of both baryon removal with adiabatic expansion and tidal stripping is extremely powerful, capable of transforming an initially incompatible dwarf into one that agrees with the entire Local Group dSph population.
- (v) Dwarfs undergo continual mass removal and reduction in v_{\max} at each pericentre passage. These values do not converge even after 6 Gyrs of evolution.
- (vi) Tidal radius over scale radius, r_t/r_s , is an important parameter for understanding the potential mass and v_{\max} loss of a dwarf. If r_t/r_s is less than four, satellites may become substantially disrupted, depending on the number of times they orbit their host.

ACKNOWLEDGMENTS

This material is based upon work supported by the National Science Foundation under Grant No. DGE-1144468. Some simulations were performed at the Leibniz Rechenzentrum Munich (LRZ).

REFERENCES

- Benson A. J., Frenk C. S., Lacey C. G., Baugh C. M., Cole S., 2002, *MNRAS*, 333, 177
- Blumenthal G. R., Faber S. M., Flores R., Primack J. R., 1986, *ApJ*, 301, 27
- Bovy J. et al., 2012, *ApJ*, 759, 131
- Boylan-Kolchin M., Bullock J. S., Kaplinghat M., 2011, *MNRAS*, 415, L40
- Boylan-Kolchin M., Bullock J. S., Kaplinghat M., 2012, *MNRAS*, 422, 1203
- Brooks A. M., Kuhlen M., Zolotov A., Hooper D., 2012, preprint (arXiv:1209.5394)
- Brooks A. M., Zolotov A., 2012, preprint (arXiv:1207.2468)

- Bullock J. S., Kravtsov A. V., Weinberg D. H., 2001, *ApJ*, 548, 33
- Bullock J. S., Stewart K. R., Kaplinghat M., Tollerud E. J., Wolf J., 2010, *ApJ*, 717, 1043
- Busha M. T., Marshall P. J., Wechsler R. H., Klypin A., Primack J., 2011a, *ApJ*, 743, 40
- Busha M. T., Wechsler R. H., Behroozi P. S., Gerke B. F., Klypin A. A., Primack J. R., 2011b, *ApJ*, 743, 117
- Ceverino D., Klypin A., 2009, *ApJ*, 695, 292
- Colín P., Avila-Reese V., Vázquez-Semadeni E., Valenzuela O., Ceverino D., 2010, *ApJ*, 713, 535
- Colín P., Valenzuela O., Klypin A., 2006, *ApJ*, 644, 687
- Colpi M., Mayer L., Governato F., 1999, *ApJ*, 525, 720
- Dehnen W., Binney J., 1998, *MNRAS*, 294, 429
- Dekel A., Silk J., 1986, *ApJ*, 303, 39
- Di Cintio A., Knebe A., Libeskind N. I., Yepes G., Gottlöber S., Hoffman Y., 2011, *MNRAS*, 417, L74
- Diemand J., Kuhlen M., Madau P., 2007, *ApJ*, 667, 859
- D’Onghia E., Lake G., 2008, *ApJ*, 686, L61
- D’Onghia E., Springel V., Hernquist L., Keres D., 2010, *ApJ*, 709, 1138
- Eskridge P. B., 1988, *ApJ&C*, 26, 315
- Flynn C., Holmberg J., Portinari L., Fuchs B., Jahreiß H., 2006, *MNRAS*, 372, 1149
- Gerhard O., 2002, *SSRv*, 100, 129
- Ghigna S., Moore B., Governato F., Lake G., Quinn T., Stadel J., 1998, *MNRAS*, 300, 146
- Gnedin N. Y., Kravtsov A. V., 2006, *ApJ*, 645, 1054
- Gnedin O. Y., Ceverino D., Gnedin N. Y., Klypin A. A., Kravtsov A. V., Levine R., Nagai D., Yepes G., 2011, preprint (arXiv:1108.5736)
- Gnedin O. Y., Hernquist L., Ostriker J. P., 1999, *ApJ*, 514, 109
- Gnedin O. Y., Kravtsov A. V., Klypin A. A., Nagai D., 2004, *ApJ*, 616, 16
- Governato F. et al., 2010, *Nat*, 463, 203
- Governato F. et al., 2012, *MNRAS*, 422, 1231
- Grebel E. K., Gallagher J. S. I., Harbeck D., 2003, *AJ*, 125, 1926
- Guo Q., White S., Li C., Boylan-Kolchin M., 2010, *MNRAS*, 404, 1111
- Gustafsson M., Fairbairn M., Sommer-Larsen J., 2006, *PhRvD*, 74, 123522
- Kallivayalil N., Besla G., Sanderson R., Alcock C., 2009, *ApJ*, 700, 924
- Karachentsev I. D., 2005, *AJ*, 129, 178
- Karachentsev I. D., Karachentseva V. E., Sharina M. E., 2005, *Proc IAU Symp 198, Near-fields cosmology with dwarf elliptical galaxies, Switzerland*, p. 295
- Kazantzidis S., Lokas E. L., Callegari S., Mayer L., Moustakas L. A., 2011, *ApJ*, 726, 98
- Klimentowski J., Lokas E. L., Kazantzidis S., Mayer L., Mamon G. A., 2009, *MNRAS*, 397, 2015
- Klimentowski J., Lokas E. L., Kazantzidis S., Prada F., Mayer L., Mamon G. A., 2007, *MNRAS*, 378, 353
- Klimentowski J., Lokas E. L., Knebe A., Gottlöber S., Martinez-Vaquero L. A., Yepes G., Hoffman Y., 2010, *MNRAS*, 402, 1899
- Klypin A., Gottlöber S., Kravtsov A. V., Khokhlov A. M., 1999a, *ApJ*, 516, 530
- Klypin A., Kravtsov A. V., Valenzuela O., Prada F., 1999b, *ApJ*, 522, 82
- Klypin A., Zhao H., Somerville R. S., 2002, *ApJ*, 573, 597
- Komatsu E. et al., 2011, *ApJS*, 192, 18
- Koposov S. et al., 2008, *ApJ*, 686, 279
- Koposov S. E., Yoo J., Rix H.-W., Weinberg D. H., Macciò A. V., Escudé J. M., 2009, *ApJ*, 696, 2179
- Kravtsov A. V., 1999, PhD thesis, New Mexico State Univ.
- Kravtsov A. V., 2010, *AdAst*, 2010, 8
- Kravtsov A. V., Gnedin O. Y., Klypin A. A., 2004, *ApJ*, 609, 482
- Kravtsov A. V., Klypin A. A., Khokhlov A. M., 1997, *ApJS*, 111, 73
- Li Y.-S., Helmi A., 2008, *MNRAS*, 385, 1365
- Li Y.-S., White S. D. M., 2008, *MNRAS*, 384, 1459
- Lokas E. L., Kazantzidis S., Mayer L., Callegari S., 2010, *ASSP, Environment and the Formation of Galaxies: 30 years later*, p. 229
- Lovell M. R. et al., 2012, *MNRAS*, 420, 2318
- Madau P., Diemand J., Kuhlen M., 2008, *ApJ*, 679, 1260
- Mashchenko S., Couchman H. M. P., Wadsley J., 2006, *Nat*, 442, 539
- Mashchenko S., Wadsley J., Couchman H. M. P., 2008, *Sci*, 319, 174
- Mayer L., 2005, *Proc IAU Symp 198, Near-fields cosmology with dwarf elliptical galaxies, Switzerland*, p. 220
- Mayer L., Governato F., Colpi M., Moore B., Quinn T., Wadsley J., Stadel J., Lake G., 2001, *ApJ*, 559, 754
- Mayer L., Kazantzidis S., Mastropietro C., Wadsley J., 2007, *Nat*, 445, 738
- Metz M., Kroupa P., Theis C., Hensler G., Jerjen H., 2009, *ApJ*, 697, 269
- Moore B., Diemand J., Madau P., Zemp M., Stadel J., 2006, *MNRAS*, 368, 563
- Moore B., Ghigna S., Governato F., Lake G., Quinn T., Stadel J., Tozzi P., 1999, *ApJ*, 524, L19
- Navarro J. F., Eke V. R., Frenk C. S., 1996a, *MNRAS*, 283, L72
- Navarro J. F., Frenk C. S., White S. D. M., 1996b, *ApJ*, 462, 563
- Navarro J. F., Frenk C. S., White S. D. M., 1997, *ApJ*, 490, 493
- Navarro J. F., Steinmetz M., 1997, *ApJ*, 478, 13
- Oh S.-H., de Blok W. J. G., Brinks E., Walter F., Kennicutt R. C. J., 2011, *AJ*, 141, 193
- Okamoto T., Frenk C. S., 2009, *MNRAS*, 399, L174
- Okamoto T., Gao L., Theuns T., 2008, *MNRAS*, 390, 920
- Parry O. H., Eke V. R., Frenk C. S., Okamoto T., 2012, *MNRAS*, 419, 3304
- Peebles P. J. E., 1984, *ApJ*, 277, 470
- Peñarrubia J., Benson A. J., Walker M. G., Gilmore G., McConnachie A. W., Mayer L., 2010, *MNRAS*, 406, 1290
- Peñarrubia J., McConnachie A. W., Navarro J. F., 2008a, *ApJ*, 672, 904
- Peñarrubia J., Navarro J. F., McConnachie A. W., 2008b, *ApJ*, 673, 226
- Peñarrubia J., Navarro J. F., McConnachie A. W., Martin N. F., 2009, *ApJ*, 698, 222
- Peñarrubia J., Pontzen A., Walker M. G., Koposov S. E., 2012, *ApJ*, 759, L42
- Pontzen A., Governato F., 2012, *MNRAS*, 421, 3464
- Quinn T., Katz N., Efsthathiou G., 1996, *MNRAS*, 278, L49
- Read J. I., Pontzen A. P., Viel M., 2006a, *MNRAS*, 371, 885
- Read J. I., Wilkinson M. I., Evans N. W., Gilmore G., Kleyna J. T., 2006b, *MNRAS*, 367, 387
- Read J. I., Wilkinson M. I., Evans N. W., Gilmore G., Kleyna J. T., 2006c, *MNRAS*, 366, 429
- Ricotti M., Gnedin N. Y., 2005, *ApJ*, 629, 259
- Sakamoto T., Chiba M., Beers T. C., 2003, *A&A*, 397, 899
- Smith M. C. et al., 2007, *MNRAS*, 379, 755
- Somerville R. S., 2002, *ApJ*, 572, L23
- Taffoni G., Mayer L., Colpi M., Governato F., 2003, *MNRAS*, 341, 434
- Taylor J. E., Babul A., 2001, *ApJ*, 559, 716
- Tikhonov A. V., Klypin A., 2009, *MNRAS*, 395, 1915
- Tissera P. B., White S. D. M., Pedrosa S., Scannapieco C., 2010, *MNRAS*, 406, 922
- Tollerud E. J., Bullock J. S., Strigari L. E., Willman B., 2008, *ApJ*, 688, 277
- Trujillo-Gomez S., Klypin A., Primack J., Romanowsky A. J., 2011, *ApJ*, 742, 16
- Vogelsberger M., Zavala J., Loeb A., 2012, *MNRAS*, 423, 3740
- Wang J., Frenk C. S., Navarro J. F., Gao L., Sawala T., 2012, *MNRAS*, 3369
- Watkins L. L., Evans N. W., An J. H., 2010, *MNRAS*, 406, 264
- Wilkinson M. I., Evans N. W., 1999, *MNRAS*, 310, 645
- Xue X. X. et al., 2008, *ApJ*, 684, 1143
- Zeldovich Y. B., Klypin A. A., Khlopov M. Y., Chechetkin V. M., 1980, *Sov. J. Nucl. Phys.*, 31, 664
- Zolotov A. et al., 2012, *ApJ*, 761, 71